Densities of hemp shiv for building: From multiscale characterisation to application

Philippe Glé, Thibaut Lecompte, Arthur Hellouin de Ménibus, Hélène Lenormand, Santiago Arufe, Camille Chateau, Vanessa Fierro, Alain Celzard

Densities of hemp shiv for building: from multiscale characterisation to application

Philippe Glé[1], Thibaut Lecompte[2*], Arthur Hellouin de Ménibus[3,4], Hélène Lenormand[5], Santiago Arufe[5], Camille Chateau[6], Vanessa Fierro[7], Alain Celzard[7]

[1]UMRAE, CEREMA, Univ Gustave Eiffel, IFSTTAR, F-67035 Strasbourg, France

[2] Univ. Bretagne Sud, UMR CNRS 6027, IRDL, F-56100 Lorient

[3] Eco-Pertica, Hôtel Buissonnet, 61340 Perche-en-Nocé, France

[4] French National Association of Short Distribution Network Hemp Producers (Association Nationale des Chanvriers en Circuits Courts), France

[5] UniLaSalle, Univ. Artois, ULR 7519-Transformations & Agro-ressources, Normandie Université, F-76130 Mont Saint Aignan, France

[6] Laboratoire Navier, Ecole des Ponts ParisTech, Univ Gustave Eiffel, CNRS, 77455 Marne-la-Vallée, France

[7] Université de Lorraine, CNRS, IJL, F-88000 Epinal, France

*Corresponding author: thibaut.lecompte@univ-ubs.fr

Abstract

This paper concerns the packing of plant particles (hemp shiv) used for building applications and aims to quantify skeletal, particle and packing densities and associated porosities. These parameters were measured on hemp particles as a case study and were used to assess the physical behaviour of this material in terms of water adsorption and absorption, mechanical compression and thermal and acoustic behaviours. A number of experimental methods have been used to characterise these parameters including fluid and powder pycnometry, mercury intrusion and X-ray computed tomography, leading to robust and complementary results as a function of particle size and level of aging by immersion in water. It was concluded that smaller particles are

characterised by higher packing and particle densities, while aged particles present a strong evolution of their microstructure, which is visible through lower packing and particle densities and higher skeletal density. By comparing these experimental results with physical property characterisations, correlations were found between water absorption and open porosity, compression behaviour and the three density scales, and between acoustic dissipation and intra- and inter-particle porosities.

Keywords: bio-based aggregates; building materials; density; porosity; microstructure; acoustics; mechanics; thermal properties

1. Introduction

Due to environmental considerations, bio-based aggregates for building construction have been increasingly studied and applied in the past three decades. Bio-based aggregates are mainly by-products, ground during a de-fibration or harvesting process, such as hemp, flax, sunflower, rice, corn, barley or lavender. They are sold on the market as raw materials, in the form of packed elongated and flaky particles, from a few millimeters to 4 cm long, with the exception of sunflower pith. The main assets of these aggregates for building applications are their plant origin and their high porosity. As a crop product, bio-based aggregates act as a carbon sink and then limit the greenhouse effect due to their use in construction and building (Ingrao et al., 2015; Pittau et al., 2018; Lecompte, 2019; Zieger et al., 2020). Their high porosity gives bio-based building materials a high level of thermal, acoustic and vapor diffusion performances. These particles have numerous variabilities (Viel et al., 2018). This is due to, firstly, the difference in species, soil composition in the fields, weather, cultivation practices and fertilisation, harvesting, grinding and sieving processes (Lenormand et al., 2017) and, secondly, the heterogeneity of measurement protocols (Amziane and Collet 2017; Lenormand et al., 2018).

Among all plant particles that can be used in buildings, hemp shiv is the material on which scientific studies and real building works have most focused on, due to the developments of hemp-lime bio-based concrete in the early 90s (Amziane and Arnaud, 2012; Amziane and Collet, 2018). Historically, hemp was cultivated for fibres. Shiv comes from the woody part of the hemp stem, and it is increasingly commercialised as a fibre by-product. It can be used alone as a raw material, to insulate ceilings for example. It can be used for floating floor applications using a thin layer of hemp shiv to level a surface. It can also be used with a binder (lime, cementitious binder or earth) as a bio-based composite, to insulate walls, floors and roofs of buildings.

In France, hemp is mainly cultivated from April to September. The harvest time depends on weather conditions and on the technical itinerary followed by the farmer. First, the seeds might be collected. Then the straw is cut and left on the ground for 1 to 4 weeks for the retting process. During retting, the plant matter is slightly degraded by microorganisms (Ribeiro et al., 2015), which facilitates defibration operations (the separation of shiv and fibres). The retting process is aborted when the weather conditions are mild enough to bale the straw or to chop the hemp directly in the field. Afterwards, the hemp is stored in a rainproof warehouse to prevent particles and fibres from being degraded due to prolonged or repeated contact with water. Hemp shiv might encounter humid conditions again if it is mixed with a binder. It can be exposed to humid conditions for a few days to several months depending on the building methods and working conditions. After storage, hemp is defibred and then screened to extract shiv from the fibres. Different shiv granulometry can be obtained, with particle lengths ranging from 4 to 20 mm, according to the French National Association of Short Distribution Network Hemp Producers.

The present study focuses on density and porosity mainly for two reasons. Firstly, because density is a method for characterising batches of raw particles. Secondly, because density and porosity are key characteristics for analysing either the thermal, acoustical or mechanical behaviour of plant particles alone or mixed with a binder:

- Thermodynamics: Irrespective of the type of building material, it is well known that thermal conductivity is strongly correlated with its density. Both the particle density and the inter-particle porosity affect their hygrothermal behaviour. Studies have been carried out to model the thermal conductivity of hemp shiv as a raw material or mixed with a binder. In a study on lime-hemp concrete, only the total porosity is used in the modelling (Collet and Prétot, 2014). Some authors (Cerezo, 2015) proposed a self-consistent homogenisation method relating the average particle density, the average particle conductivity and the density of the packing. Other authors (Tran-Le, 2019) also developed a scale homogenisation approach for lime-hemp composites, using three densities: the apparent density of the packing, that of the particles, and that of the particle cell walls (skeleton). In the same way, (Nguyen et al, 2010; Nguyen et al., 2016; Tronet et al., 2016) distinguished the intra-particle porosity (encompassing close and open porosity) and the inter-particle porosity.
- Acoustics: the acoustic behaviour of hemp shiv and hemp concrete has also been investigated in (Cerezo, 2005; Glé et al., 2012; Kinnane et al., 2016; Fotsing et al., 2017) at two main scales of porosity: inter-particle pores and intra-particle pores. It has been shown by (Glé et al, 2012) that not all of them contribute to sound dissipation, and a new scale of porosity, called “acoustic porosity” has been proposed.
- Mechanics: hemp shiv packing, in bulk or mixed with a mineral binder, can be considered as a granular matter. Then, their compression behaviour (in the fresh state as well as after hardening in the case of hemp concrete), is strongly related to their packing characteristics: porosity or solid volume fraction. Tronet et al. (2014, 2016) have used several models from the literature, each one relating the compression pressure (or the compressive strength) to the volume, itself depending on compactness, density or porosity, for instance (Walker, 1923; Cooper and Eaton, 1962; Jones, 1960).

To summarise, the granular packing of plant particles, as a raw material or mixed with a mineral binder, presents different scales of porosity and the same packing density can be achieved in

different ways. For example, hemp shiv containing residual fibres will be lighter in the bulk state. In this case, to reach the same density as a fully defibred shiv, it has to be compressed. Then, the two kinds of packing, even with the same density, will show different structures, porosities, percolation paths and local contacts, which will affect its acoustic, hydrothermal and mechanical performances. It is then crucial to have a thorough knowledge of the densities, at the three different scales of the packing: global apparent density, average particle density and particle skeleton density. These different scales are illustrated in Fig. 1.

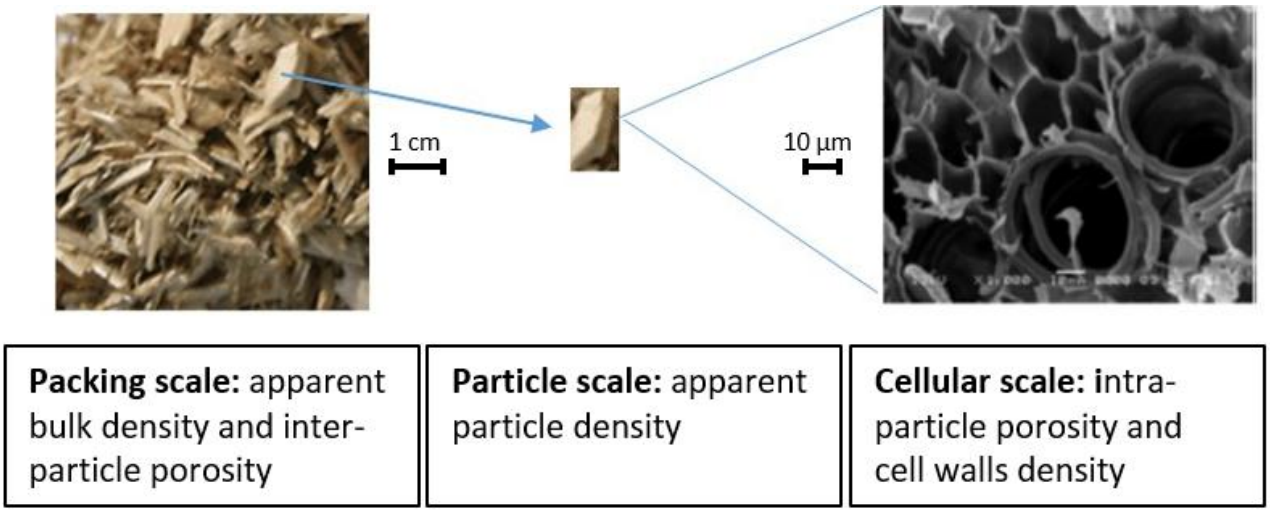

Figure 1. The three different scales for studying hemp shiv packing

The density, compactness and porosity parameters, and their interrelations are defined in Table 1, and Eq. (1) to Eq. (8).

115 *Table1: Nomenclature and definition of the main parameters of the present study*

Parameter	Definition	[unit]	and related formulas	
M	Total mass of a hemp shiv packing	[kg]		
V_T	Total, or bulk volume of a plant particles packing	[m^3]		
V_{VT}	Total volume of void space (irrespective of size) in the packing	[m^3]		
V_P	Total apparent volume of particles	[m^3]		
V_{VP}	Volume of void space inside the particles	[m^3]	$V_{P=} V_T - V_{VT} + V_{VP}$	(1)
ρ_B	Bulk density : apparent density of a packing	[kg/m^3]	$\rho_B = M / V_T$	(2)
ρ_P	Particle density: apparent density of particles	[kg/m^3]	$\rho_P = M / V_P$	(3)
ρ_S	Particle skeleton density	[kg/m^3]	$\rho_S = M / (V_P - V_{VP})$	(4)
φ_T	Total porosity inside a plant particle packing	[−]	$\varphi_T = V_{VT} / V_T = 1-\rho_{B/}\rho_S$	(5)
φ_P	Intra-particle porosity	[−]	$\varphi_P = V_{VP} / V_P = 1-\rho_{P/}\rho_S$	(6)
φ_I	Inter-particle porosity	[−]	$\varphi_I = (V_{VT} - V_{VP})/ V_T = 1-\rho_{B/}\rho_P = (\varphi_T - \varphi_P)/(1 - \varphi_P)$	(7)
φ_{acou}	Acoustic porosity: porosity contributing to sound dissipation	[−]		
C_B	Bulk compactness, or total solid volume fraction of the aggregate packing	[−]	$C_B = 1-\varphi_{T=} \rho_B / \rho_S$	(8)

116

117 The measurement procedure to assess the bulk density predominantly affects the results: in this
118 state, the loading method of the packing has an impact on the measurement results (vibrations,
119 shocks, pouring, manual or mechanical compression). Several studies have been carried out to
120 identify how to measure the particles bulk density in a robust and repeatable way (Nozahic, 2012;
121 Amziane and Collet, 2017; Evrad, 2008; Fares, 2014). On one hand, the bulk density is not an

intrinsic property of an individual shiv since it encompasses the closed and open porosities inside hemp shiv particles plus a given amount of air between the particles, which depends on the measurement method. On the other hand, the bulk density gives some indications on the batch composition in terms of particle shape and size (a smaller particle size results in a higher bulk density) and of the purity level after the defibration process (the remaining fibres lower the density). Then, the literature values for the bulk density of hemp shiv range from 50 to 155 $kg.m^{-3}$ (Nguyen, 2010; Laborél-Prénéron et al., 2018; Amziane and Collet, 2018; Lenormand et al., 2017).

At the particle scale, some attempts have been made to estimate the density of shiv, called "particle density". Nguyen (2010) measured the density of the woody core of hemp stems by weighing and measuring the volume of a de-skinned and defibred stem. Values around 260 $kg.m^{-3}$ have been found. Pierre and Carin (2019), with a similar protocol, found 265±15 $kg.m^{-3}$. The main problem at this scale is the variability of this material, first from particle to particle in the same batch, but it also depends on the species and the crop practices. A significant variability is even observable in the same stem, as reported by Glé (2013) through acoustic measurements on different types of shiv from the bottom, middle or top of hemp stems, and by Beaugrand et al. (2014).

At the skeleton scale, the measurements are generally achieved with a gas pycnometer. The size order of cell wall density of hemp shiv, obtained in this way, is 1450 $kg.m^{-3}$ (Amziane and Collet, 2018). This value is close to the density of the holo-cellulose 1540 kg/m^3 (Ehrnrooth ,1984) that mainly composes the cell walls of hemp shiv.

There are still a number of key questions concerning the measurements, the values and the variability in the densities of plant particles, such as:

- If the measurement of particle density has been made on pristine, full hemp stem samples collected directly after harvesting, then they have not undergone retting, grinding and sieving during their life cycle. The outer cell wall would be mechanically damaged (by grinding), and the inner cells could be biochemically damaged (by retting).

- If the differentiation between open and closed intra-particle porosities has never been made, it may have some consequences on performances, particularly in acoustics.
- And even if some clear recommendations have been made by a RILEM technical committee concerning the measurement of bulk density, it still remains difficult to interpret the results from different density measurement methods from a physical point of view.

Thus, the aim of this paper is to provide an overview of the densities and porosities of plant particles used as building aggregates, focusing on: what are the different porosities, how to measure them and how to use them to predict their properties in building applications. The case study uses a commercialised hemp shiv in two different states: the raw (initial) shiv being compared to a shiv that has been wetted over a long period of time.

The particles are described, followed by experimental measurements (batch density, pycnometry, mercury porosimetry and X-ray tomography). Finally, the results are analysed and compared, and discussions are based on applications in different contexts (mechanics, hydrothermal behaviour and acoustics).

The main contributions and originalities of this paper lie in: the measurement of particle densities by correlating tomography measurements and powder pycnometry in the same batches, to provide reliable values; the comparison of skeletal densities depending on the life cycle of the aggregate, and of its chemical composition; the understanding of what a bulk state is, depending on the conditioning process.

2. Materials and Methods

2.1. Hemp shiv: morphological and chemical description

2.1.1. Description of hemp shiv samples

A commercial hemp shiv, lightly retted (yellow colour) was used in this study. Homogenous samples of particles have been sampled from a 200 L bag of shiv following RILEM TC 236-BBM procedures. This raw shiv is referred to as L in this paper.

To investigate the potential effects of the particle size of hemp shiv on densities, a fraction of this raw shiv was preserved as it was, while the rest was sieved in order to artificially produce other shiv with different particle sizes. These shiv are referred to as *Lxy* where *x* and *y* are respectively the lower and the higher sizes (in mm) of the associated sieves. Three shiv were thus produced: *L12*, *L24* and *L4+* (particles that do not pass through the 4mm sieve).

Shiv can dramatically change in terms of microstructure depending on their environment. In consideration of this, it was decided to study raw samples (*L*, *L12*, *L24* and *L4+)* as well as samples artificially aged through immersion in water.

The aged samples consisted of shiv immersed for 8 days in laboratory temperature conditions (T=20°C ± 2°C) using nets ballasted in buckets filled with 10 L of mains water. The duration of 8 days was chosen on the basis of previous results of Glé and Gourlay (2015) showing that the skeletal density of immersed shiv increases significantly during this time and then stabilises. This duration can also be considered as a state of extreme aging in the fields where hemp is cultivated.

After 8 days, the water had a very strong smell of fermentation. The drying of these samples was carried out in two steps: first, the samples were kept for several days in the open air, then the samples were placed in an oven at 50°C until their mass stabilised at 0.01%. After stabilisation, the

samples were then sent to the different laboratories for measurements. These modified samples of shiv are named *LxyM*.

2.1.2. Particle size distribution

The particle size distribution of original shiv (*L, L12, L24 and L4+*) and modified shiv (*LM, L12M, L24M and L4+M*) was determined by image analysis using the protocol described by Amziane and Collet (2017). Images of each sample were taken using an optical system (Keyence, CA-MX500M) by placing the particles on a plate (CA-DSW15). The particle size was then determined employing a scale factor of 0.0609 mm/pixel. At least 1000 particles of each sample were measured. This number allows guaranteeing a certain accuracy of measurement. Indeed, a study based on 10 various hemp shiv ~~in~~ (Glé, 2013) showed that the analysis of 1000 particles led to an uncertainty for particle width and length distributions strictly lower than 5%, and confirmed previous results by Ceyte (2008).

Fig. 2 shows the accumulated particle frequency of length and width for all studied samples. The four size distributions are correlated with the sampling sieves, in terms of length and width. The larger size of the corresponding sieve used results in a particle size distribution with a higher percentage of larger and longer particles. For example, the corresponding width for 50% of cumulated particle frequency increased from 1.2 (*L12*) to 1.8 mm (*L4+*), *L* having the smallest (1 mm).

Regarding the effect of the immersion of hemp shiv in water for 8 days (*LM, L12M, L24M, L4+M*) compared to the same sampling without immersion, particle size distributions show a higher percentage of large particles. The characteristic dimensions of the shiv (mean and median of distributions) presented in Table 2 increase from 15 to 22% in length and from 7 to 21% in width, which highlights a significant swelling of particles caused by water.

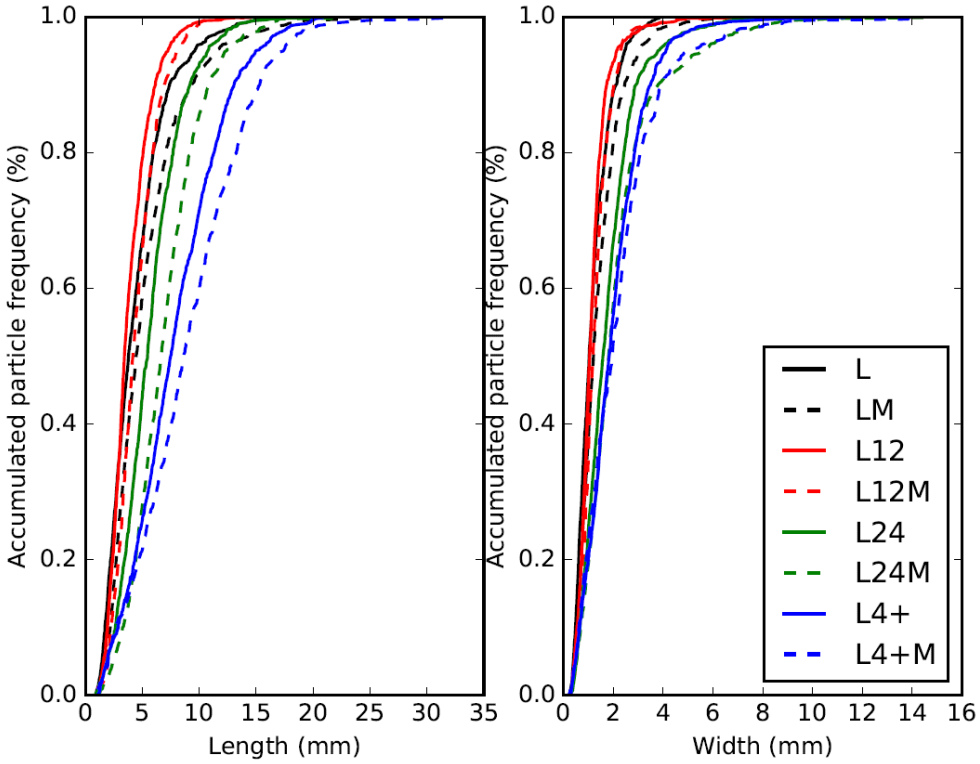

Figure 2. Particle size distribution of hemp shiv in length and width, characterized through 2D-image analysis

Table 2. Characteristic dimensions of shiv, deduced from 2D-image analysis (mean and standard deviation values are derived from a lognormal distribution)

	Length (mm)					***Width (mm)***				
Shiv	***Median***	***Mean***	***Std Dev***	***Mean (log(L))***	***Std Dev (log(L))***	***Median***	***Mean***	***Std Dev***	***Mean (log(W))***	***Std Dev (log(W))***
L	*3.78*	*4.36*	*2.58*	*3.72*	*1.77*	*1.02*	*1.17*	*0.66*	*1.00*	*1.74*
LM	*4.45*	*5.24*	*3.31*	*4.43*	*1.77*	*1.20*	*1.40*	*0.92*	*1.16*	*1.84*
L12	*3.42*	*3.82*	*1.76*	*3.46*	*1.57*	*1.05*	*1.15*	*0.63*	*1.03*	*1.61*
L12M	*4.16*	*4.48*	*1.88*	*4.10*	*1.54*	*1.17*	*1.27*	*0.62*	*1.14*	*1.60*
L24	*5.46*	*5.70*	*2.69*	*5.06*	*1.67*	*1.58*	*1.77*	*1.10*	*1.49*	*1.82*
L24M	*6.63*	*6.93*	*3.06*	*6.23*	*1.63*	*1.81*	*2.14*	*1.58*	*1.72*	*1.95*
L4+	*7.47*	*7.87*	*3.98*	*6.74*	*1.83*	*1.83*	*2.00*	*1.21*	*1.66*	*1.91*
L4+M	*8.62*	*9.01*	*4.75*	*7.55*	*1.93*	*1.95*	*2.21*	*1.64*	*1.72*	*2.08*

2.1.3. Chemical composition

The chemical composition of hemp shiv (with contents of ash, lignin, cellulose, hemicellulose and soluble matter) was determined according to the Van Soest method (NF V 18-122). To carry out this measurement, hemp shiv (previously dried at 40ºC until obtaining a constant weight) were milled using a micro impact mill (Culatti, Switzerland). The rotor speed was adjusted to 7, and a standard sieve of 1 mm mesh size was used.

Hemp shiv L and LM show very close standard compositions (g/100 g dry solid). These values presented in Table 3 are in line with the data in the literature (Amziane and Arnaud, 2012; Amziane and Collet, 2017; Cappelletto et al., 2001; Beaugrand et al., 2014; Viel et al., 2018; Delannoy et al. 2020). Scatter between studies might come from the variability in particle batches due to plant variability or different retting conditions. It could also come from the measurement procedures (Van Soest, TAPPI) or from the way compositions are calculated by percentage.

The method used for the determination of the chemical composition is based on the calculation of the percentages of each component by their elimination during the experiment, which gives the relative proportion of each component in the sample. This can explain the fact that, for example, hemicellulose and lignin had slightly higher values for LM hemp shiv compared to L hemp shiv. In this context, it must be taken into account that LM has a mass loss due to immersion, which leads to lower quantities of all compounds compared to L hemp shiv in an absolute scale. Taking into account the mass loss caused by water immersion for 8 days, it seems that the main affected compounds may be soluble matter and ashes. For example, Thygens et al. (2013) found a 38 % mass loss on hemp stems after immersion in water at 35°C for 4 days. Water treatment generated a decrease in hemicellulose and pectin (soluble) contents. Differences in plant matter (hemp stems for Thygens et al. (2013), hemp shiv for this study), conditions of treatment (temperature, duration) and probably the degree of retting explain the variability.

Table 3. Chemical composition of the different shiv samples, and values found in the literature (Amziane and Arnaud, 2012; Amziane and Collet, 2017; Cappelletto et al., 2001; Beaugrand et al., 2014; Viel et al., 2018; Delannoy et al. 2020)

g/100g dry solid	Soluble matter	Hemicellulose	Cellulose	Lignin	Ashes
L	9.5±1.2	16.8±2.5	60.8±2.2	10.4±1.1	2.5±0.1
LM	8.1±0.5	18.6±0.5	59.4±0.9	12.03±0.3	2.0±0.1
Literature	5.1 – 12	9 - 25.9	34.5 - 54.9	9 - 28	1.2 - 6.5

2.2. Microstructure and density characterisation methods

2.2.1. Methods for measuring the bulk density

Four methods for the measurement of bulk particle density have been explored in the literature:

- **Trimmed density**: shiv is gently placed in a cylinder, progressively dropping the particles in the form of a light rain, then the particles are levelled and the cylinder is weighed (Nozahic, 2012).
- **Apparent density**: shiv is placed in a cylinder and overturned ten times, then the packing volume and mass are measured (Amziane and Collet, 2017).
- **Tapped density**: shiv is placed in a cylinder, and the container is tapped on a rigid surface a given number of times (or alternatively a weight is dropped from a given height on the table where the cylinder is placed). Hemp shiv is progressively compacted up to a saturation point (Evrard, 2008; Fares, 2014). Two methods based on an automatic process have been used to measure this density, firstly using a MICROMERITICS GeoPyc 1360 pycnometer (GeoPyc density), and secondly a QUANTACHROME AT-6 Autotap device (Autotap density). With the Geopyc, the sample chamber is rotated and agitated while a force is applied to the sample. The measurements were repeated 12 times (or for 12 cycles) and carried out in a cell with an internal diameter of 12.7 mm and subjected to a piston applying a force of 5N. With the Autotap, the samples were shaken with a given tapping rate, tapping force and cylinder diameter, to obtain a stabilised packing. The measurements were carried out in a 100 cm^3 test tube (internal diameter 2.5 cm and height

of the graduations 18 cm) and subjected to 4500 consecutive shakes or strokes (speed 260 strokes per minute, displacement in the height direction of 2 mm).

- **Compacted**: shiv is compacted manually using a wooden structure, up to saturation point following the protocol of Chiasson-Poirier et al. (2020).

The first three methods measure a “random loose packing” (RLP) while the latter measures a “close packing” (CP). The random loose packing corresponds to a momentum state of the packing for which the percolation and the contacts between particles only compensate for gravity. The different random loose packing methods are not equivalent since the difference between tapped and loose density gives some indication about how particles flow (Lam et al., 2007). The close packing supposes a higher energy of compaction to rearrange the particles and reach an optimum of compactness without particle deformation. For example, the RLP compactness of uniform rigid spheres packing is about 0.555 while its CP compactness is 0.645 (Onoda and Liniger, 1990).
All these bulk measurement methods were carried out with shiv at equilibrium in laboratory conditions (20 - 23 °C / 50%HR). For trimmed, apparent and compacted densities, glass cylinders were used with a 16 cm inner diameter and a height of 32 cm.

2.2.2. Pycnometry

Pycnometry is the technique of measuring the volume of a solid by placing a sample in a cell of a certain and very precise volume, and measuring the quantity of fluid that can be placed in it afterwards. Depending on whether or not this fluid can penetrate the porosity of the solid, *i.e.*, whether it is a gas or a fine powder, the volume of the solid skeleton or the envelope of the solid can be determined. By knowing the sample mass, its skeletal (true) or apparent (envelope) density can be deduced.

The true density, or skeletal density, of the hemp particles, after being dried at 60°C for at least 24h under vacuum, was investigated with a MICROMERITICS Accupyc II 1340 pycnometer using two different inert gases, helium (He) and nitrogen (N_2). These methods were applied to all the

292 samples, on the raw particles as well as on powdered particles, with the aim of observing possible
293 differences due to closed porosity in the raw particles. Mercury intrusion porosimetry has also been
294 used to estimate the skeletal density (See Section 2.2.3).

295 The Accupyc device, equipped with a 10 cm^3 cell (internal diameter 1.85 cm and height 3.8 cm)
296 without insert, was used as follows: a filling pressure of 1.4 bars (19.5 psig) was first applied with
297 an equilibrium rate of 0.005 psig / min. The analysis stopped when the volume obtained from the
298 measurement cycle deviated by less than 0.1% from the average of the volumes of the last five
299 cycles. Each density determination thus requires around fifty cycles. After the measurements were
300 carried out, the samples were recovered and ground for 45 min in the 250 mL agate bowl of a
301 Retsch PM100 planetary mill. By doing so, the particle size was reduced to between 100 and 500
302 µm, and the measurements were repeated under the same conditions.

303 The envelope density of the particles was evaluated after being dried for 24h at 60°C under
304 vacuum with a MICROMERITICS GeoPyc 1360 pycnometer (and with mercury intrusion
305 porosimetry, see Section 2.2.3), using a cylindrical cell of volume 7.6 cm^3 (inner diameter 1.27 cm
306 and length 6 cm). The larger particles (length 1 cm, width 0.3 - 0.5 cm, except for the smaller L12
307 sample) were selected for this type of measurement, as they are more representative in cases
308 where a significant part of closed porosity is present.

309 The characteristics, targets and limitations of these various pycnometry approaches is summarised
310 in Table 4.

311

Table 4 : Pycnometer parameters and assumed density

Hemp particles size/shape	Fluid	Measured or deduced parameter	Experimental device	Experimental validity/ limitation
Aggregate (Shiv particles)	Dry Flo powder (Micro-Meritics®)	Apparent (« envelope » particle density)	Geopyc 1346 Sample volumes between 0.3 cm^3 and 0.8 cm^3	Typical range of sizes : 100 – 200 µm > capillary pore diameter
	Helium (He)	Open porosity	Accupyc II 1340 Volume: 10 cm^3	Kinetic diameter of N_2: 0.364 nm; Kinetic diameter of He: 0.26 nm (Breck ,1974)
	Nitrogen (N_2)			
	Air			
Ground powder (100<X<500 µm)	Helium (He)	Particle walls density, deduction of closed porosity by comparison with the skeletal density measured on raw particles.	Accupyc II 1340 Volume: 10 cm^3	Size of the ground powder (be sure to not have remaining closed porosity)

2.2.3. Porosimetry by mercury intrusion

Mercury porosimetry involves forcing mercury to penetrate the porosity of a porous solid. As mercury is a non-wetting liquid, it is necessary to increase its pressure for it to intrude into smaller and smaller pores. At low pressure, the mercury follows the contours of the material sample; its volume and therefore its apparent density can be deduced. However, it can never be certain that the mercury penetrated all the pores at the pressure applied. On the contrary, at very high pressure, when the mercury is supposed to have penetrated all the accessible porosity, the skeletal density of the material can be deduced. Here, another assumption must be made,

according to which there is no narrower porosity remaining that mercury could have penetrated if the device had been able to access higher pressures.

Mercury porosimetry is therefore an interesting technique because it can make it possible to determine these two types of density, but subject to assumptions that are difficult to verify, except by comparing the results with gas and powder pycnometry techniques. Any significant difference in the results will then be indicative of the limitations of mercury porosimetry. This method can in particular have difficulty in separating interparticle porosity from intraparticle porosity. In addition, the necessarily limited pressure that the porosimeter can reach prevents the intrusion into the narrowest pores, producing significant errors in the case of nanoporous solids.

Mercury porosimetry is nevertheless a valuable technique since it is possible to deduce the distribution of pore sizes from it. The corresponding calculation is based on the knowledge of the relationship between the pressure and intruded pore diameter (known as the Washburn equation), but is again based on questionable assumptions, including the fact that pores are considered to be cylindrical and that they are gradually intruded from the widest to the narrowest when the pressure increases. However, nothing prevents large porous volumes being downstream of narrow pores. These pores, called "ink-bottle" pores, then lead to the overestimation of the volume of narrow pores and to the underestimation of the larger ones, and consequently the diameters determined by the method are not pore diameters but neck diameters, *i.e.* diameters of the restrictions giving access to real pores. This is well known in the case of lignocellulosic biomass, where tracheids have a diameter in the order of 10 µm and are accessible only by pits that ensure the connections between them, which have a diameter in the order of 1 µm.

In this work, an Autopore IV Micromeritics device has been used. Prior to analysis, the samples were dried at 60°C in a vacuum oven, and then placed in a glass penetrometer (total volume of 3.54 cm^3 with a 3.13 cm^3 reservoir). The particles were introduced by hand and the penetrometer gently agitated to allow dense stacking. The procedure was repeated as many times as necessary to introduce the maximum number of particles. The experiments were performed in two steps: low

pressure (0.001–0.24 MPa) and high pressure (0.24–414 MPa). The low- and high- pressure equilibration time setting was 10 seconds.

2.2.4. X-ray computed tomography

X-ray computed tomography (XRCT) is a non-destructive imaging technique, which is now widely used in materials science. It provides 3D images of objects that reveal their internal structure (see e.g. (Brisard et al., 2020) for detailed information on the method). It has been used, for example, to visualise the microstructure of hemp shiv (Ceyte, 2008; Jiang et al., 2018; Bennai et al., 2018). Here, we propose to obtain the 3D envelope of the particles individually, to estimate their apparent volume and then deduce their apparent density from a mass measurement.

Image acquisition was performed using an XRCT laboratory scanner (Ultratom from RX-Solutions). Several hemp shiv of different sizes, were imaged together to minimise the number of image acquisitions. In order to make image processing easier, the particles were separated from each other by placing them into individual compartments made from adhesive tape strips covered with expanded polystyrene (EPS) beads with a diameter of about 1 mm. Tape strips were sewn with cotton thread to form the compartments. It was necessary to use such low attenuating materials to minimise the absorption contrast with hemp shiv, and then to avoid streak artefacts on the images. Once set, the particles were put vertically into a plastic container.

Two scans were necessary to examine 29 particles. The magnification (*i.e.* the voxel size) was chosen to limit the number of image acquisitions whilst still having a sufficient resolution to characterise the envelope accurately. Each scan lasted about 12 hours (image acquisition settings are given in Appendix). Note that the exposure time needs to be long enough to improve the signal-to-noise ratio of the images and thus to overcome the low X-ray attenuation of the hemp shiv. The final 3D images have been reconstructed with a voxel size of 12 µm, using the X-Act software provided by the manufacturer of the XRCT device, and regions of interest were cropped around each particle. As illustrated in Fig. 3a and the cross-sections provided as supplementary

material, the images reveal the heterogeneous microstructure of the particles, including growth rings. Although the largest vessels can be seen, the spatial resolution is not fine enough to characterise porosity. Finally, the images were processed to select the particle only (segmentation) and to estimate its apparent volume, as described in Appendix. As illustrated in Fig. 3, the envelope of the particle is correctly extracted, retaining most of the fine details.

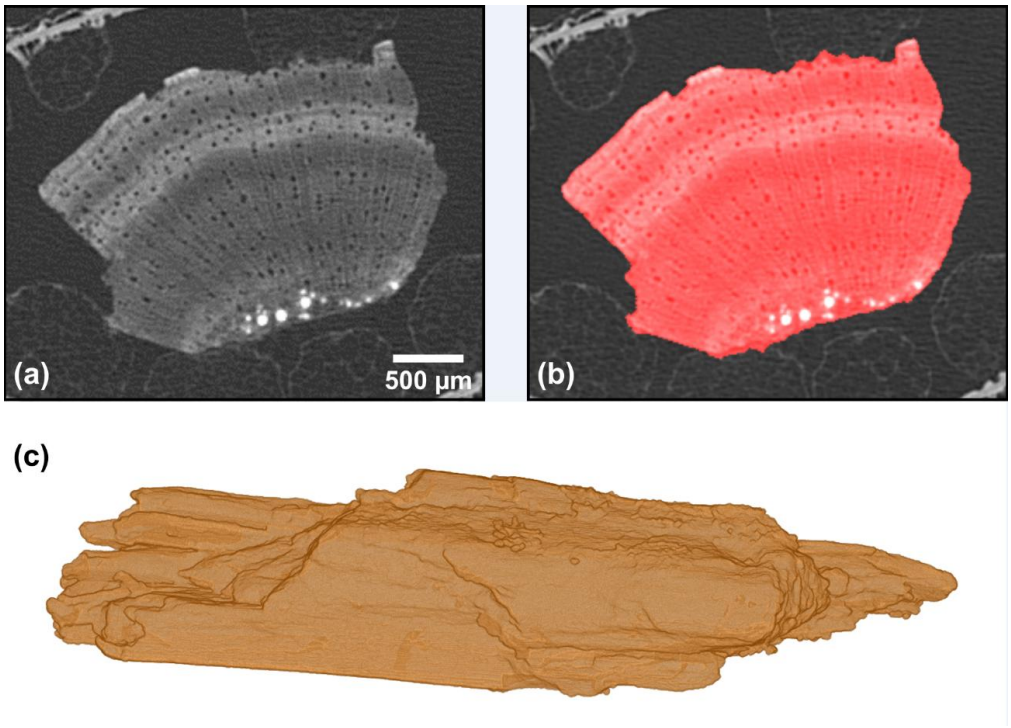

Figure 3. Extraction of the envelope of a L24 particle (approx. 11 mm long) : (a) cross-section of the XRCT image, (b) result of image segmentation superimposed on the original slice, (c) 3D rendering of the envelope, obtained using Volume Viewer plugin included in Fiji (Schindelin et al., 2012).

An analysis was conducted on two *L12*, one *L24* and one *L4+* particles to estimate the sensitivity of the volume measurement to image processing parameters. Their values were varied in ranges resulting in a qualitatively good segmentation. Thus, the volume measurement was found to be mainly sensitive to grey level thresholding with an uncertainty ranging from 1% to 4.5%, without any correlation with particle sizes. Furthermore, preliminary tests were conducted on a few

particles with a finer resolution (voxel size of 4 µm) and showed the discrepancy to be less than 2%. Thus, the results take into account of a 5% uncertainty in the measurement of the volume of all particles. In addition, each particle was weighed with an analytical balance with a precision of 100µg, which produces an uncertainty of measurements of 11% for the smallest *L12* particle, of less than 2.5% for *L24/L24M* particles, and less than 1% for *L4+/L4+M* particles. Finally, the apparent densities ρ_P (as defined in Table 1, Eq. (3)) and the corresponding uncertainties have been estimated for each particle individually and grouped by type of shiv (Table 5), where *L/LM* refers to all particles, all sizes included. The overall uncertainties reach 10%, 6.5%, 5% and 6% for *L12/L12M, L24/L24M, L4+/L4+M* and *L/LM* particles, respectively. Average particle densities are discussed in the following sections of the paper but densities per particle are available in supplementary material for information.

2.3. Methods to characterise the physical properties of hemp shiv

2.3.1. Study of water sorption

Water sorption isotherms of hemp shiv were determined at 23°C using a Dynamic Vapour Sorption machine (SPS-Sorption Test System, proUmid), using nitrogen as the carrier gas in order to control relative humidity. Each sample was at least measured in duplicate (219 ± 34 mg as average sample weight). Different equilibrium points were determined corresponding to a fixed relative humidity (RH): 0, 5, 10, 15, 20, 30, 35, 50, 75, 85 and 90% for adsorption experiments, and 0, 15, 30, 35, 50, 75, 85, and 90% for desorption experiments. The samples used for the adsorption experiments were previously dried at 40°C in an oven until reaching a constant weight. The samples for desorption were previously exposed to a relative humidity of 90% for hydration until they reached a constant weight.

412 Guggenheim-Anderson-de Boer (GAB) (Van den Berg and Bruin, 1981) model was used to fit the
413 experimental water sorption data (equilibrium moisture content, X_{eq}, and relative humidity, RH) Eq.
414 (9):

415 $$X_{eq} = \frac{X_m KCRH}{(1-KRH)(1-KRH+CKRH)} \quad (9)$$

416 where X_m is the monolayer moisture content (kg water/kg dry solid), C (dimensionless, -) and K
417 (dimensionless, -) are parameters related to the heat of sorption of the multilayer in the GAB
418 model.

419 The water absorption kinetics of different samples were determined at 5, 15, 60, 480, 1444 and
420 2880 min. Samples (~1 g) previously dried at 40ºC until reaching a constant weight were placed in
421 water using a tea strainer ball, then removed, filtered under a vacuum filter to remove excess water
422 from the surface of the material, and dried in an oven at 105ºC until reaching a constant weight to
423 determine the mass loss during water absorption (SS, kg solid loss/ kg dry solid). SS was
424 calculated as follows, Eq. (10):

425 $$SS = \frac{Dry\ mass\ before\ immersion\ (kg) - Dry\ mass\ after\ immersion\ (kg)}{Dry\ mass\ after\ immersion\ (kg)} \quad (10)$$

426

427 ### 2.3.2. Acoustics

428 Every hemp shiv in this study has been characterised following the method developed in (Glé et
429 al., 2012).

430 The experimental data were obtained through an AcoustiTube impedance tube, having a diameter
431 of 10 cm and a [50; 2000Hz] frequency range. The three-microphone method without cavity,
432 developed by Iwase et al. (1998), was applied to measure the sound absorption coefficient α as
433 well as the intrinsic dynamic properties (dynamic density ρ and dynamic bulk modulus K). For each

shiv, three densities of the mixes have been tested, ranging between 70 and 150 kg.m^{-3} depending on the particle size distribution. For each density, the acoustic measurements were repeated three times.

The effective acoustic porosity, referred to here as φ_{acou}, was evaluated from the acoustic measurements. From φ_{acou}, it was then possible to evaluate for a given shiv the associated density ρ_{acou} so that $\varphi_{acou} = 1 - \frac{\rho_B}{\rho_{acou}}$. The initial assumption made ~~in~~ (Glé et al., 2012) was that $\rho_{acou} \approx \rho_P$.

2.3.3. Bulk compressive behaviour

To measure the compressive behaviour of the hemp shiv granular packing, a steel cylinder die with an inner diameter of 30mm and a height of 170mm was used. The die was placed under a hydraulic press fitted with a force transducer (capacity of 500 kN), and a displacement sensor measured the position of the press crossbeam.

A lower punch (40mm in height) was inserted into the die and the shiv was poured in, with a protocol similar to that of trimmed density measurements (Section 2.2.1), so the initial height of the granular packing was 130mm. Then, an upper punch of 30mm in height and a plain steel-cylinder-spacer of 100mm in height were set up.

The compression was then controlled with displacement and speed, in three sequences:

- a movement of 60 mm with a rate of 40 mm/min;
- a movement of 40 mm with a rate of 20 mm/min;
- a movement with a rate of 6mm/min, up to a compressive force of 110 kN (upper punch compressive stress of 155 MPa).

This protocol is very close to the protocol developed by Tronet et al. (2014, 2016).

The compressive stress is calculated with the force given by the transducer, plus the weight of the upper punch and the spacer. The height of the sample during compression is deduced from the crossbeam position and is corrected, using a preliminary blank made on the stack of punches, spacer and transducer only. The size order of the stiffness of this solid stack is 5 µm/MPa, which becomes significant for the highest compressive stresses.

At the end of compression, the shiv packing is stiff and cohesive enough to be pulled out, and weighed. From the weight and initial height of the sample, an initial bulk density can be deduced, and then the evolution of the packing density versus upper punch compressive stress can be graphically represented.

2.3.4. Thermal properties in the bulk state

The samples of hemp shiv were dried at 60°C before being tested. Two different protocols were carried out on the shiv packing: guarded hot plate and hot disk.

For the guarded hot plate, the measurements were performed at 23°C with a temperature difference between the plates of 20°C using a HFM 436/3/1E Lambda (NETZSCH). The sample size was 7x30x30 cm. The supplier indicates that the uncertainty on the measurement is 1 to 3%, and the repeatability is better than 0.25%.

Hot disk measurements were performed at room temperature (21°C) using a HOT DISK TPS 2500 S. Hemp shiv was poured into a 1 liter plastic cylinder with a slot for the probe. The supplier indicates that the uncertainty on the measurement is lower than 5%, and the repeatability is better than 1%.

3. Results and discussion

3.1. **Characteristics of hemp shiv**

3.1.1. Densities

All results are shown in Table 5, from the packing scale (ρ_B) to the particle skeleton scale (ρ_S). A comparison of the approaches is first proposed scale by scale, then, the differences between samples related to immersion and particle size effects are analysed.

Table 5 : Bulk, particle and skeletal densities of hemp shiv scale by scale

	Bulk density ρ_B (kg.m^{-3})				***Particle density ρ_P (kg.m^{-3})***				***Particles skeleton density ρ_S (kg.m^{-3})***				
	Geopyc	***Autotap***	***Trimmed***	***Apparent***	***Compacted***	***Hg***	***Geopyc***	***XRCT***	***Acou***	***N_2***	***Hg***	***He***	***He ****
L	*137*	*133*	*99*	*108*	*140*	*290*	*330*	*311*	*478*	*1150*	*1211*	*1413*	*1460*
LM	*118*	*105*	*82*	*84*	*109*	*282*	*210*	*245*	*443*	*1450*	*1144*	*1441*	*1455*
L12	*150*	*128*	*105*	*136*	*159*	*305*	*326*	*286*	*515*	*1190*	*1247*	*1420*	*1457*
L12M	*108*	*101*	*83*	*87*	*107*	*246*	*254*	*252*	*469*	*1490*	*1238*	*1445*	*1450*
L24	*120*	*125*	*105*	*104*	*138*	*281*	*299*	*318*	*502*	*1170*	*1154*	*1430*	*1456*
L24M	*84*	*91*	*80*	*85*	*105*	*230*	*242*	*262*	*441*	*1480*	*1270*	*1454*	*1452*
L4+	*117*	*103*	*94*	*104*	*136*	*218*	*286*	*311*	*447*	*1140*	*1266*	*1407*	*1455*
L4+M	*91*	*79*	*64*	*73*	*102*	*236*	*274*	*241*	*396*	*1460*	*1260*	*1445*	*1450*

* ***milled/ground particles***

The five methods used to evaluate bulk density lead to values ranging between 64 and 159 kg.m^{-3}. The two automatic methods for tapped density (Geopyc and Autotap) give similar results. These values are compared to the manual methods in Fig. 4. Considering the other values, it appears that trimmed densities are systematically the lowest, and that compacted densities are generally the highest. The apparent density method lies between the trimmed density and the tapped density. Such differences in values from one technique to another were expected, given the uncertainty with this type of measurement and the rather d ifferent methods for obtaining them.

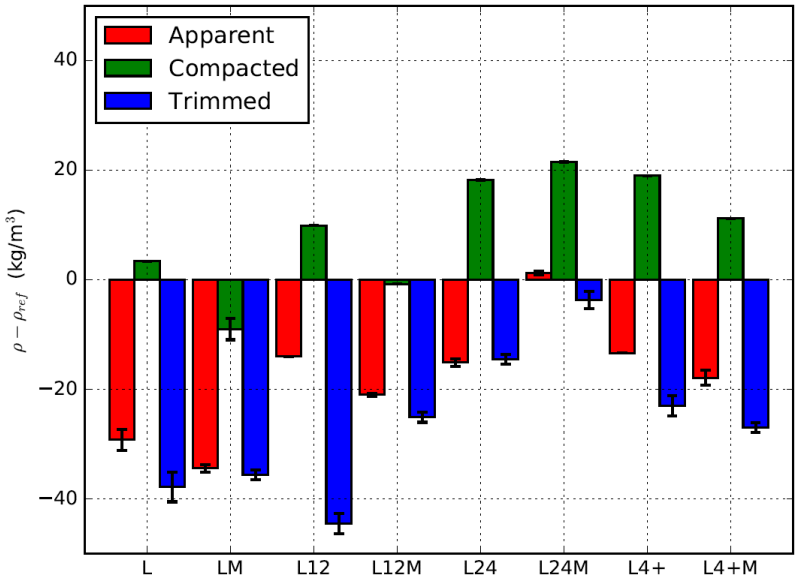

Figure 4. Bulk density of hemp shiv. Differences between manual and automatic methods (here "reference density" corresponds to the average of the results from the Geopyc and Autotap methods)

The particle densities evaluated using mercury intrusion and Geopyc, range between 210 and 330 kg.m^{-3} and are relatively close, especially for the batches without large particles (L12, L12M, L24, L24M) for which differences lower than 6% were observed. It can be observed that the values obtained from Hg porosimetry are generally the lowest, suggesting that part of the inter-particle porosity was not completely filled by mercury at the low pressure used for the measurement. Regarding XRCT measurements, densities are also relatively close to Geopyc and Hg values. Differences with Geopyc values are the lowest, ranging from 1% to 12% (all batches except L/LM). Nevertheless, the final result could not be conclusive because of the significant variations observed from one particle to another (see Fig. 5 and supplementary material), with relative standard deviations ranging from 7% to 33% depending on the shiv. Two extreme values were observed (as detailed in Appendix) that are very different from the general trend. They illustrate the variability in the particle densities, but they seem to be only rare occurrences. The number of observed particles was probably not enough to be statistically representative of the shiv, contrary to Geopyc

measurements, which were performed on larger sets of particles (cell of volume 7.6 cm^3). Therefore, at this scale, it was decided to focus mainly on Geopyc results for the remainder of the paper.

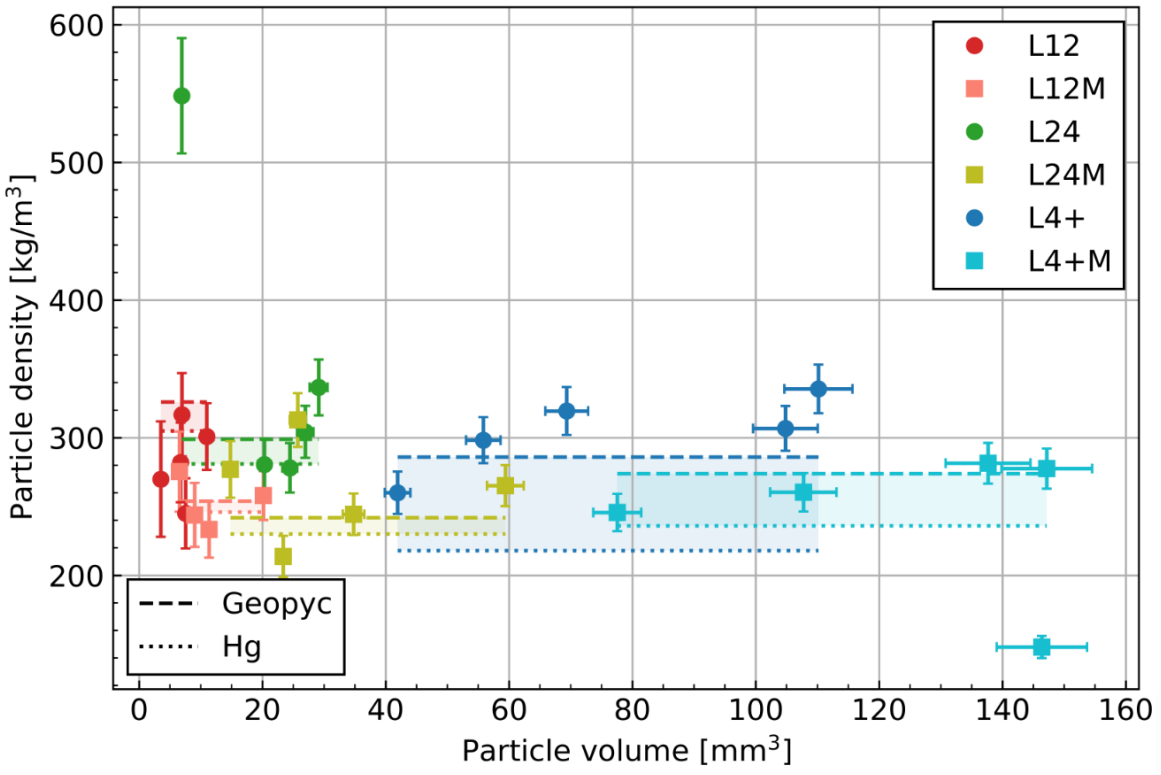

Figure 5. Particle densities estimated by tomography compared to mercury intrusion and Geopyc measurements.

Finally, the skeletal density of the particles was analysed using four approaches. Values are in the range of [1100 - 1500 $kg.m^{-3}$] and globally respect the ranking $\rho_{N2} < \rho_{Hg} < \rho_{He} < \rho_{He\ powder}$. Hg intrusion values, at the highest pressure, 414 MPa, are indicated for information and are between N_2 and He values. At such a pressure, the Washburn equation shows that the narrowest pores that can be intruded have a diameter of only 3.6 nm.

On this basis, many features can be observed by comparing these results between reference and immersed samples. At the loose packing scale, a decrease ranging between 14% and 30% of the initial value in the density due to immersion is clearly visible, whether measured with Geopyc or

532 Autotap. This is associated to a dimensional swelling of particles which has also been observed
533 elsewhere in previous studies (Castel et al., 2016; Delannoy et al., 2018). Concurrently, the
534 envelope densities of the particles decreased after immersion, which is again related to this
535 swelling effect. These results were confirmed by the three techniques (powder pycnometry, Hg
536 porosimetry and X-ray computed tomography) used for measuring them. At the skeleton scale, an
537 increase in the measured density is clearly visible after immersion (on the basis of N_2 and He
538 pycnometry). This change has already been pointed out in other studies (Glé and Gourlay, 2015;
539 Delannoy et al., 2018) and is a consequence of the degradation of the microstructure, resulting in
540 an opening of pores that were initially not accessible. The measurements on finely ground samples
541 ("He*" column in Table 5) show that the density in this case is remarkably constant, with a value of
542 1455 ± 5 $kg.m^{-3}$, irrespective of whether the materials were aged in water or not. However,
543 differences between immersed and raw samples are visible in various ranges with He and N_2
544 pycnometry, and the values obtained with N_2 were either equal or lower than those obtained with
545 He. N_2 is a molecule with a kinetic diameter of 0.364 nm, whereas He is a monoatomic gas with a
546 kinetic diameter of 0.26 nm (Breck, 1974). These differences thus suggest either that a significant
547 fraction of extremely narrow pores, smaller than about 0.4 nm, were opened in some materials
548 after immersion, or that He atoms were able to diffuse to poorly accessible porosity. It is useful to
549 recall here that the diffusivity of He is typically 10 times higher than that of other common gases,
550 and He can therefore migrate in many materials that remain impervious to other gases.

551 Plant matter can be considered as a composite composed of different macromolecules each
552 having specific true density. The literature provides a true density of about 1541-1549 kg/m^3 for
553 holocellulose, 1490-1800 kg/m^3 for hemicellulose (Ehrnrooth, 1984) and 1420-1460 kg/m^3 for
554 cellulose (Sun, 2005) and 1335-1400 kg/m^3 for lignin. According to the chemical composition
555 obtained by the Van Soest method, a rough estimation of the true density of hemp shiv can be
556 deduced. The estimated values for both the L and LM samples range between 1420 and 1520
557 kg/m^3, and include the experimental result.

Concerning the size effect of the particles, the results show that the particle skeleton density is the same for all batches in a given state (raw or after immersion). It also appears that smaller particles are denser (in terms of particle density). This can be related to the original position of the particles in the stem, and that bigger particles coming from the lower part are more porous and thus less dense. In addition, the two automatic methods (Geopyc and Autotap) agree on the bulk density of the associated mixes, showing higher densities for smaller particles, which is directly related to a more compact stacking of the particles. However, this trend is not confirmed by the tomography approach in Fig. 5, where it is observed that there is no trend in density evolution as a function of particle volume.

3.1.2. Pore size distribution

The results of mercury intrusion are presented in three ways in Fig. 6.

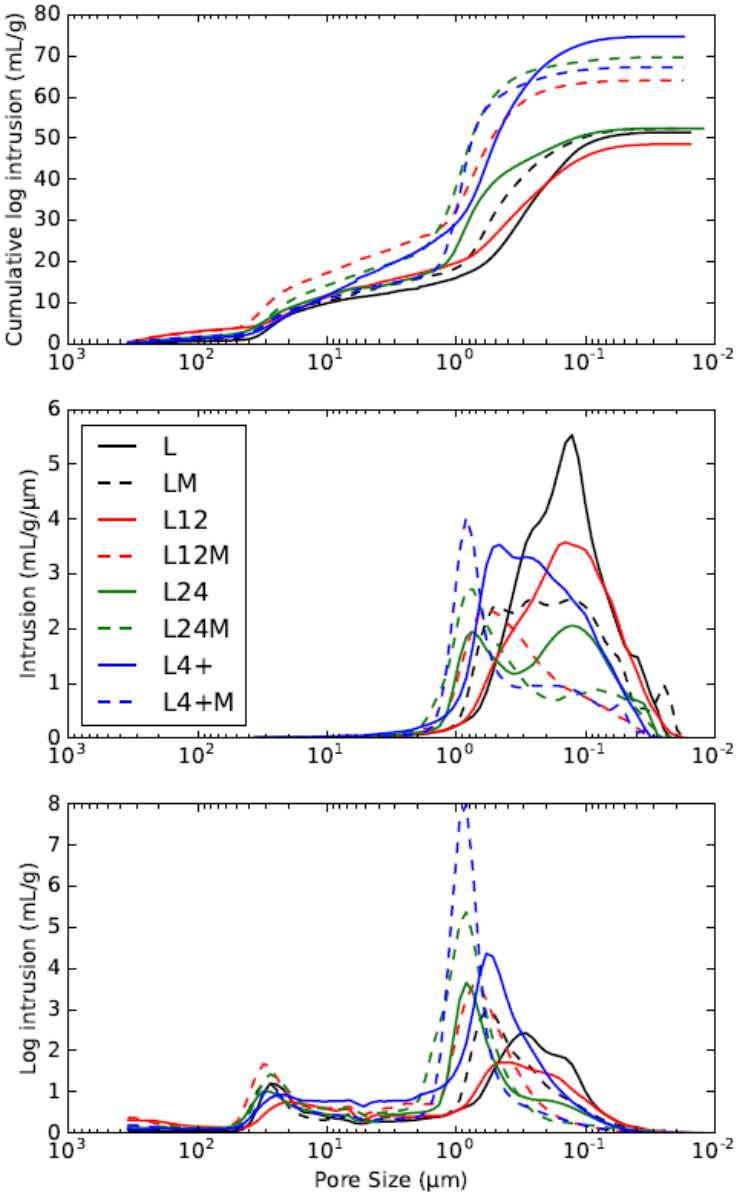

Figure 6. Mercury intrusion porosimetry : Cumulative intrusion in mL/g (top, the extrusion curves are not shown), differential intrusion in mL/g/µm (middle) and differential log intrusion in mL/g (bottom) as a function of pore size in µm

Pore size is presented here in decreasing order to underline the process of pressure increase during the measurement. The first representation is a cumulative curve of Hg Intrusion, where horizontal pseudo-plateaus represent different families of pores. The extrusion curves are not shown for clarity, but are perfectly horizontal indicating that all the intruded mercury has remained trapped in the porosity of the materials. In other words, all the mercury remains trapped because of the narrow necks giving access to most of the pores, which the mercury can only pass through under increasing pressure, but cannot cross in the other direction when the pressure decreases. This observation confirms the ink bottle-pore character of these materials, which is moreover a well-known morphological characteristic of the vascular network of wood and related plants. Only a fraction of the lumens indeed have an open side, and can therefore be directly intruded by mercury, but the vast majority of them are only accessible (and therefore intruded) by punctuations, typically an order of magnitude smaller in diameter. As a first approximation, the two steps observed on the intrusion curves therefore suggest that the pore size distribution is bimodal. Two other representations are differential and thus correspond to the pore size distributions. The log distribution is more responsive to larger pores (Meyer and Klobes, 1999), and clearly shows the bimodal character of the porosity, which cannot be so clearly seen in the middle of Fig. 6, due to the scale.

On this basis, these experimental results indicate two groups of pores:

- Pores between 10 and 50 µm;
- Pores between 0.02 and 2 µm.

A parallel can be drawn between these groups and the families of pores existing in hemp particles. Vessels are the bigger pores in hemp and have a dimension around 50 µm while tracheids have diameters of about 10-20 µm, and pits have diameters of 1-2 µm (Delannoy et al., 2018). However, as explained in section 2.2.3, it is important to recall that mercury intrusion tends to overestimate the volume related to small pores as soon as ink-bottle pores are present, which is more than likely the case here.

Indeed, not only is this geometry confirmed by the structure of the plant cells and the impossibility of extracting the mercury from them, but also by the fact that the samples observed after the mercury porosimetry test show no deformation, and that their weighing enables the intruded quantities measured by the device to be retrieved. This means that mercury under pressure did not alter the structure of the materials, which was to be expected given the presence of large pores and a very wide pore size distribution.

It also appears that the pores are systematically greater after immersion, which is visible through the shift of the plots towards larger pore sizes. In addition, the results show an increase of the total porosity after immersion, for all shiv except for the case of L4+. This is clearly correlated with N_2 and He pycnometry observations, and can be explained by the degradation (opening) of the microstructure after immersion.

3.2. **Physical properties of hemp shiv**

3.2.1. Water sorption

The GAB model satisfactorily fitted the experimental data (R^2>0.9996 using parameters in Table 6). Regarding the corresponding parameters, no clear difference was observed between raw and immersed samples over the whole range of relative humidity tested (*i.e., L* and *LM* shiv, Fig. 7).

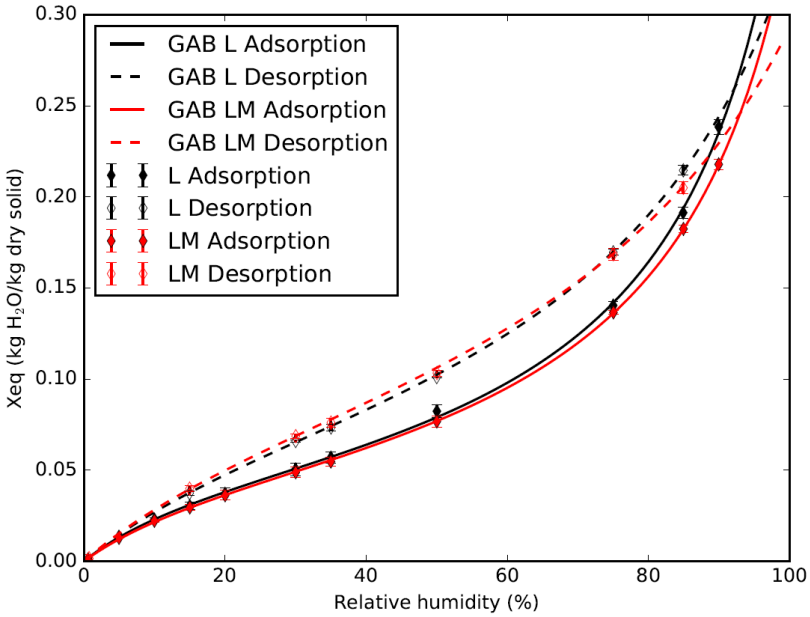

617

618 Figure 7. Adsorption and desorption isotherms of water on shiv L and LM

619

620 *Table 6 : GAB model parameters (Eq. (9)), R² are not detailed but are systematically greater than 0.99*

	Param	L	LM	L12	L12M	L24	L24M	L4+	L4+M
Adsorption	C (-)	6.9±1.0	6.2±0.8	7.4±0.7	6.5±0.7	6.6±0.9	6.6±0.8	6.2±0.7	6.7±0.8
	K (-)	0.871±0.003	0.849±0.003	0.873±0.008	0.851±0.005	0.868±0.009	0.853±0.003	0.853±0.007	0.854±0.004
	X_m (10^{-3} d.b.)*	53±1	54±1	53±2	53±1	52±1	53±1	54±1	52±1
	E_{RMS} (10^{-3} d.b.)*	2	1	2	1	2	1	1	1
Desorption	C (-)	5.2±0.6	5.2±0.9	5.3±0.2	5.1±0.6	5.0±0.2	5.0±0.6	4.8±0.4	5.0±0.8
	K (-)	0.764±0.003	0.706±0.036	0.768±0.006	0.704±0.028	0.758±0.006	0.704±0.031	0.735±0.019	0.701±0.037
	X_m (10^{-3} d.b.)*	83±5	93±7	82±0	93±6	82±3	93±6	88±3	93±8
	E_{RMS} (10^{-3} d.b.)*	2	2	1	2	2	2	2	2

621 *d.b.: dry basis, in kg water/kg dry solid

3.2.2. Water absorption by immersion

Fig. 8a shows the kinetics of water absorption (WA) for the raw samples. As can be observed, the samples with a higher percentage of small particle size (*L*) sorb water faster than the others when t ≤ 480 min. This behaviour could be related to the different tortuosity of the studied samples, which could lead to a higher absorption rate for samples with lower diffusional resistance (lower tortuosity). A similar effect was observed between treated samples.

Regarding the effect of immersion in water for 8 days on the absorption kinetics, it was observed that immersed samples had a lower capacity of water absorption compared to the raw ones (Fig. 8b). This behaviour can be explained by the loss of mass after 8 days of immersion in water by leaching and/or by the increase in open porosity ($\varphi_{N_2} = 1 - \frac{\rho_B}{\rho_{N_2}}$). As can be seen in Fig. 8b, raw samples lose more mass than samples previously immersed, indicating that those immersed have already lost mass before the water absorption kinetics analysis. This fact suggests that raw hemp shiv could have a higher number of hydrophilic compounds compared to the immersed ones due to the leaching effect, which led to a lower water retention capacity. For example, when equilibrium was achieved (2880 min) L sample had a WA of ≈ 4.3 kg water/ kg initial dry solid whereas the LM sample had a lower value (≈ 3.9 kg water/ kg initial dry solid). In addition, in Fig. 8b, it can also be seen that the rate of water absorption seems to be the same for both types of hemp shiv (constant difference between WA at each time for both types). Furthermore, it should be noted that even the samples that were previously immersed in water for 8 days continued to lose mass at 2880 min (which means 10 days of total immersion time). This result is in line with those previously published by Glé and Gourlay (2015).

a)

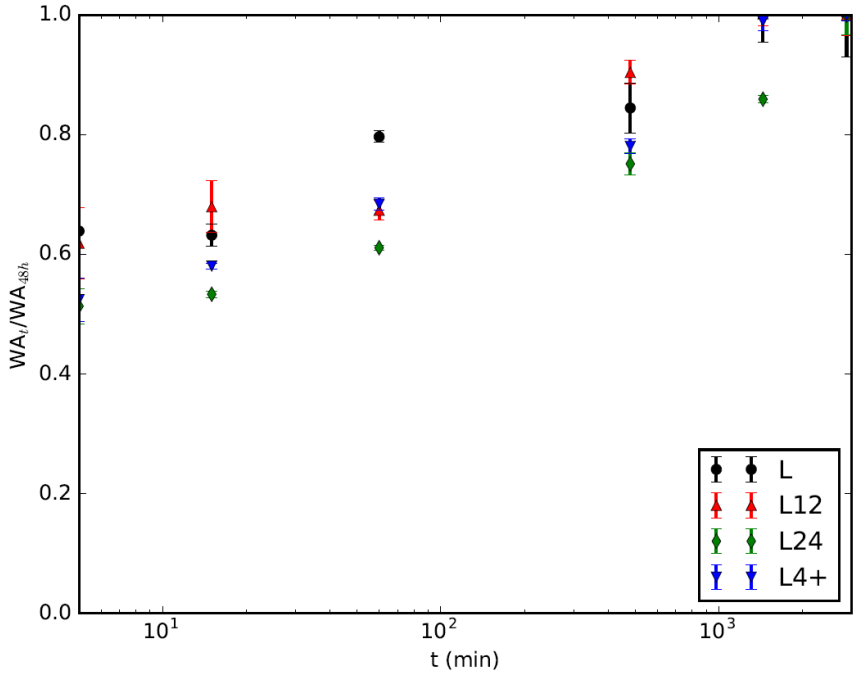

b)

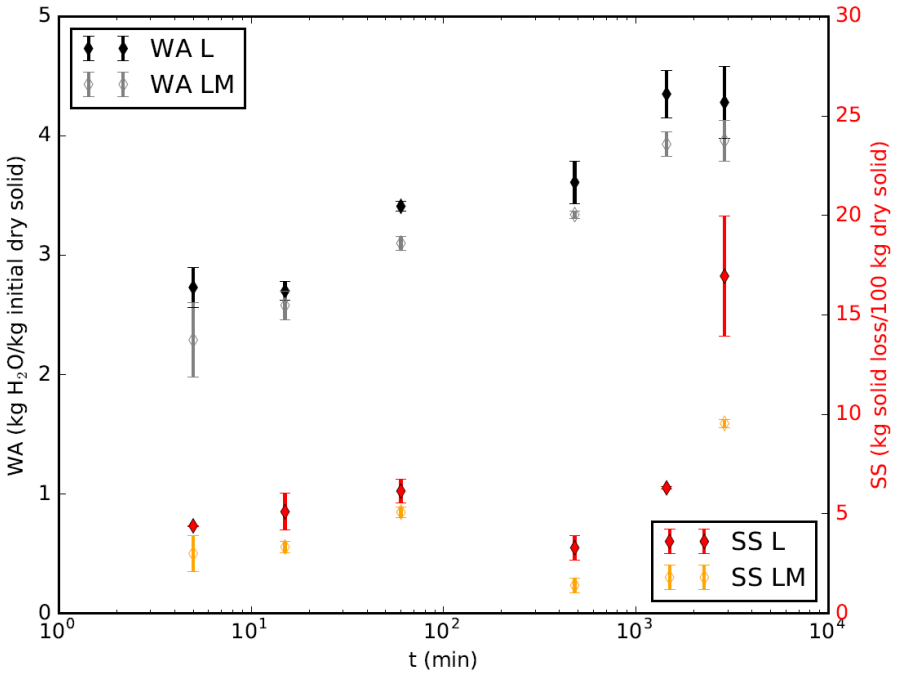

Figure 8. Water demand of hemp shiv. Comparison between raw shiv (a) and the effect of immersion on shiv (b). SS is the mass loss during water absorption defined in Eq. (10).

Finally, it should be noted that pre-immersed samples show a WA closer to the ideal behaviour than those not immersed. If it is considered that WA is the result of a complete filling of the open porosity of samples with water molecules, then:

$$WA = \frac{\varphi_{P-open} * \rho_{water}}{(1 - \varphi_{P-open})\, \rho_S} \quad (11)$$

Fig. 9 compares the theoretical WA calculated with Eq. (11) with those obtained experimentally at 48 h. Results for immersed samples (*LM, L12M, L24M, L4+M*) are quite close to this theoretical behaviour, contrary to raw samples (*L, L12, L24, L4+*). Porosity, density and particle size distributions suggest that modified samples swelled irreversibly during their immersion treatment. The fact that the WA estimation of Eq. (11) underestimates the WA for raw particles suggests that these particles are swelling, in addition to filling their open porosity with water.

On this basis, it is possible to propose a new equation for the theoretical WA accounting for swelling:

$$WA = \frac{\varphi_{P-open} * \rho_{water} * (1+s)^3}{(1 - \varphi_{P-open})\, \rho_S} \quad (12)$$

with *s* the dimensional swelling of particles, estimated at about 15% due to the shift of size distribution curves from the raw samples to modified samples (see Table 2 – the same value has been taken for the thickness as data is missing). This corrected evolution is also plotted in Fig. 9 and shows a better agreement with data on raw samples.

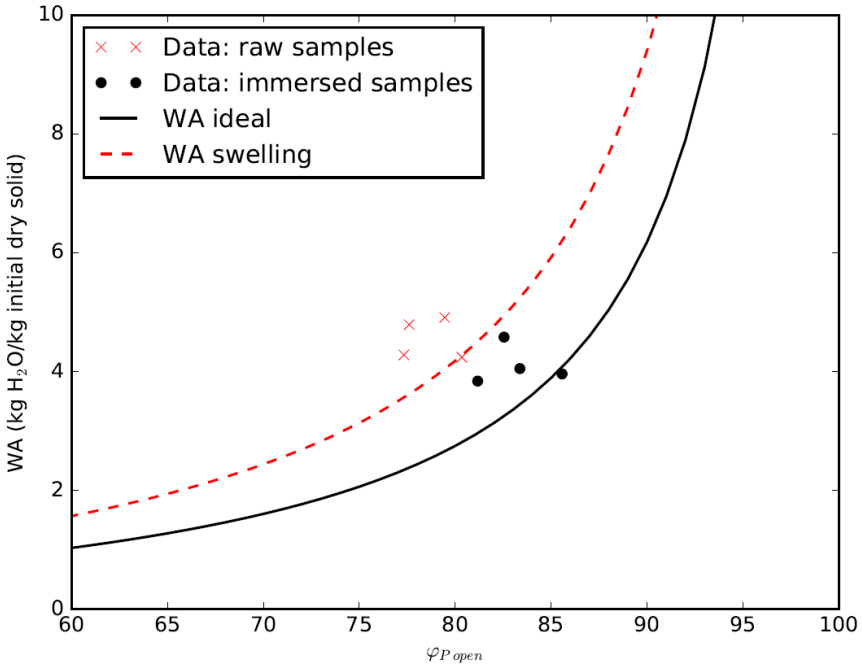

Figure 9. Comparison between measured water absorption and theoretical evolution as a function of the open porosity of particles (WA ideal Eq. (11) and WA swelling Eq. (12)).

3.2.3. Compression behaviour

The mechanisms of granular packing compression are generally distinguished in three steps, as first described by Seeling and Wülff (1946): 1. rearrangement of particles; 2. local elastic and plastic deformation of particles and 3. fragmentation of particles and new rearrangement. For this reason, Cooper and Eaton (1962) created a model that considers void filling that is dependent on pore size, *i.e.* when rearrangement and filling of small voids occur or when plastic deformation and fragmentation occur. Tronet et al. (2014) and a later study (Chiasson-Poirier et al., 2020) observe that this model is in very close agreement with the compression behaviour of bulk hemp shiv (dry or wet) and lime and hemp mixtures (dry or wet), considering only the two first steps (Eq. (13)).

$$\frac{1-C_0/C}{1-C_0} = a_1 exp(P_r/\sigma_{UP}) + a_2 exp(P_d/\sigma_{UP}) \quad (13)$$

With *C* the compactness, or solid volume fraction achieved by the compressive stress σ_{UP} applied on the upper punch (negative value). a_1 and a_2 are constants. In fact, the constants a_1 and a_2 are not independent, as theoretically, when σ_{UP} tends towards $-\infty$, *C* must tend towards 1. Then a_1+ a_2=1. C_0 is the initial compactness, which can be considered as a "trimmed" bulk compactness (C_{B-trim}) taking into account the experimental process of the present study (see section 2.3.3). In Cooper and Eaton's model, P_r and P_d are coefficients related to the pressure needed to perform the process that has the greatest probability of occurring; for instance, according to these authors, P_r = 21 MPa and P_d = 345 MPa for compacting an alumina powder. This consistently higher value for P_d indicates that filling small voids requires considerably higher pressures than filling large ones. For shiv and lime-hemp mixtures, P_d values are also ten to twenty times higher than P_r, but these values are very low compared with metal or mineral powder beds, similarly to straw particles, wet or dry, which are very flexible and compressible (Mani et al., 2004) Both rearrangement and deformation phases are easier to discern for biomass resource particles than for rigid and frictional ones. In comparison, Tronet et al. (2014) found a P_r value of 450 kPa and P_d value of about 5 MPa for the compaction of dry shiv.

By applying the hypotheses of Cooper and Eaton's modelling, it could theoretically be possible to de-correlate the two phenomena (rearrangement and deformation), and write Eq. (14), which only considers the rearrangement phase:

$$\frac{1-C_0/C_{r\infty}}{1-C_0} = \lim_{\sigma_{UP}\to-\infty}\left[a_1 exp(P_r/\sigma_{UP})\right] = a_1 \quad (14)$$

Where $C_{r\infty}$would be the rearrangement occurring under infinite pressure, without any deformation of the particles. Considering a perfect layout of the particles in the packing under infinite pressure, $C_{r\infty}$can be directly related to the particle density and the skeletal density. Similarly, C_0 can be expressed with trimmed bulk density and skeletal density, Eq. (15):

$$C_{r\infty} = \rho_P / \rho_S \quad ; \quad C_0 = C_{B-trim} = \rho_{B\text{-}trim} / \rho_S \quad (15)$$

Then Eq. (13) can be reformulated in terms of densities as follows (Eq. (16)):

$$\rho = \left[\frac{1-exp(P_r/\sigma_{UP})}{\rho_{B-trim}} + \frac{exp(P_r/\sigma_{UP})-exp(P_d/\sigma_{UP})}{\rho_P} + \frac{exp(P_d/\sigma_{UP})}{\rho_S}\right]^{-1} \quad (16)$$

The different samples of shiv were compressed using the protocol described in section 2.3.3 (Fig. 10a). The experimental curves are clearly gathered by shiv type ("pristine" *Lxy* or "modified" *LMxy*) and these bundles are distinct for compressive stresses higher than 15 MPa. At lower stresses, the initial bulk density and internal and wall-die frictions could dramatically affect the packing's compressive behaviour, as shown by Tronet et al., (2014) and Chiasson-Poirier et al. (2020). By zooming in on the experimental curves (Fig. 10b), it appears that the coarser the particles, the easier the compaction: for example, in the deformation step, *L4+* reaches a given density for a much lower pressure than *L12*, even if its initial density is lower. This can be due to two phenomena: small particles induce more particle/particle contacts than big ones and are stiffer in bending. However, modified samples (*LMxy*) reached lower densities, even though they are generally larger than pristine particles (*Lxy*). This is due to their much lower particle density (about -20%) induced by the degradation of some internal cell walls (see Figure 4 and Table 5).

The experimental results "L" and "LM" are compared to the model of Eq. (16), taking the average density values of Table 5: ρ_S=1454 kg/m^3 for each sample (column "skeleton, He*"); ρ_{B-trim}=99 kg/m^3 for L samples and 82 kg/m^3 for LM samples (column "packing, trimmed"); ρ_P=310 kg/m^3 for L samples and 245 kg/m^3 for LM samples (column "particle, Geopyc"). The only two fitting parameters of the model are P_r and P_d. The same value was taken for P_r=0.53 MPa, while the P_d values are slightly different for the two shiv samples: P_d=2.5 MPa for "L" group, and 2 MPa for "LM" group. These values are of the same order of magnitude as those of Tronet et al. (2014).

a)

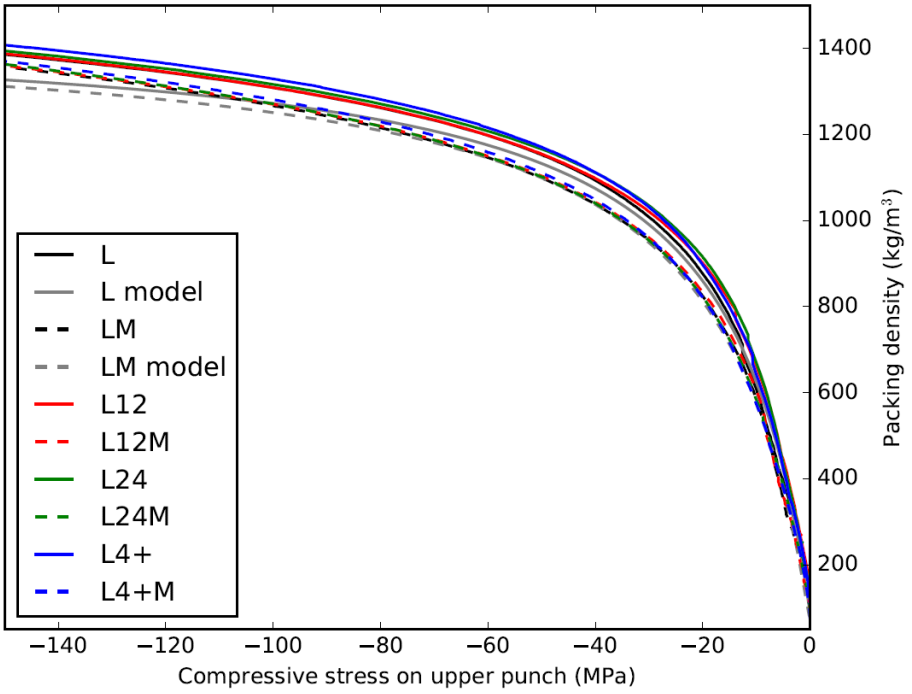

b)

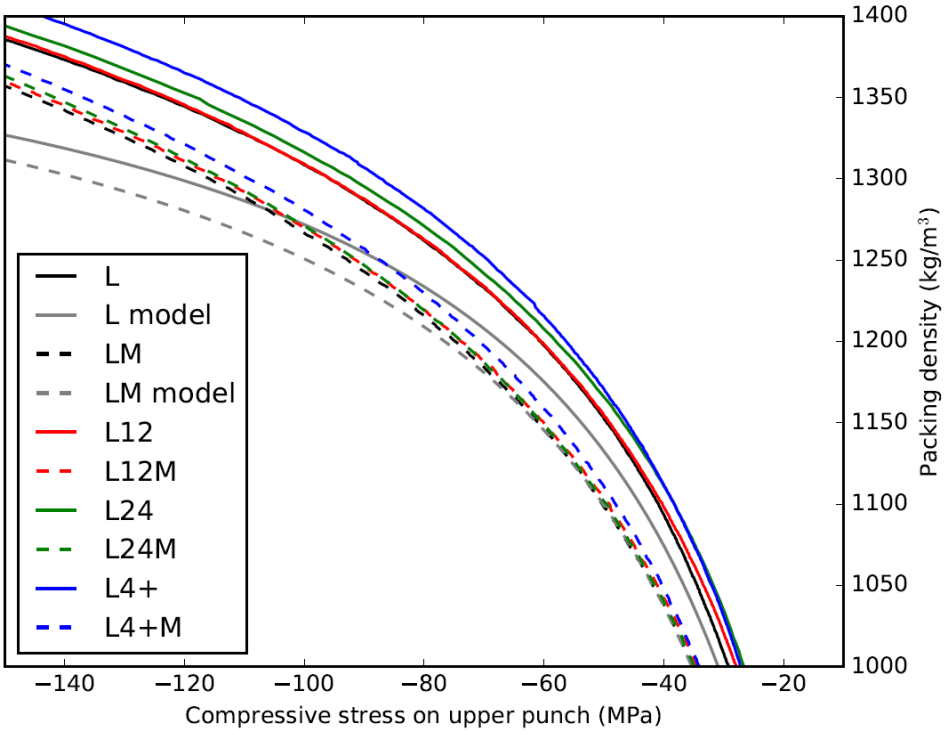

Figure 10. Left: experimental curves and the Cooper & Eaton model with P_r=0.53 MPa (model L: P_d=2.5 MPa,ρ_S=1454 kg/m^3 , ρ_{B-trim}=100 kg/m^3 , ρ_P=310 kg/m^3 ; model LM: P_d=2 MPa, ρ_S=1454 kg/m^3 , ρ_{B-trim}=80 kg/m^3 , ρ_P=245 kg/m^3); Right: zoom of the experimental values.

A fairly close agreement between the model and the experiments is observed, up to a compressive stress of about 70 MPa. In fact, to transform Eq. (14) to Eq. (16), the implicit assumption that a compactness of 1 corresponds to a density ρ_S was performed. This assumption does not take into account the compressibility of the skeleton's cell wall itself. To summarise, the successive phenomena that drive the packing behaviour in the die are firstly a rearrangement that should be achieved when $\rho = \rho_P$. Then, the deformation of the particles drives the compressive behaviour (bending at the macroscale; buckling of the cell walls and closing of the intra-porosity at the microscale) up to a density level for which the volume deformation of the cell walls themselves can no longer be neglected. The model should then be completed by considering ρ_S, which depends on the compressive stress:

$$\rho_S = \rho_{S0}(1 + \sigma_{UP} / K_S) \quad (17)$$

Where ρ_{S0} is the skeletal density in atmospheric conditions (values of Table 3), and K_S is the elastic bulk modulus of the cell walls. Beaugrand et al. (2014) measured indentation moduli from nanoindentation on the woody core of hemp stems around 9 GPa. The bulk modulus should be of the same order of magnitude. The curves of models *L* and *LM* were drawn again, varying the skeletal density as a function of compressive stress (Eq. (17)). A bulk modulus of 3.8 GPa gave the best agreement with the experimental values (Fig. 11).

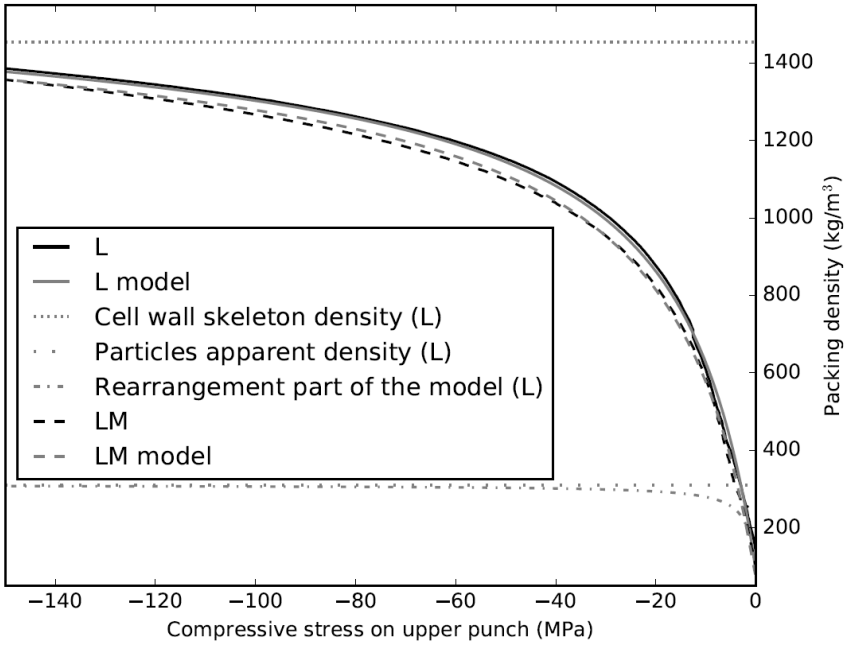

757

758 Figure 11. Compression model and experiments, considering that the cell wall density depends on
759 compressive stress (K_S =3.8 GPa).

760

761 The rearrangement part of the Cooper and Eaton model is also drawn in Fig. 11. This curve clearly
762 shows that the rearrangement phase is the driving phenomenon at the beginning of the
763 compression, and is rapidly achieved. The whole model tends asymptotically towards the cell walls
764 skeletal density.

765 The rearrangement pressure P_r found is the same for all shiv samples, and is quite similar to the
766 value found by Tronet et al. (2014). This pressure is driven by several parameters, mainly inter-
767 particle porosity and inter-particle friction. This result indicates that, irrespective of the type of shiv,
768 the porosity and the nature of the outer cell walls are sufficiently similar to drive the rearrangement
769 phase in the same way and with the same pressure levels. On the contrary, the deformation
770 pressure P_d is related to the stiffness of the particle (in flexion and compression), *i.e.,* to the particle
771 density. This explains why the P_d value is lower for LM samples than for L samples.

3.2.4. Thermal behaviour

The thermal models usually proposed for a diphasic granular packing and formulated in terms of densities are written in Eq. (18) to (21) :

- Series Model:

$$\lambda_B = \frac{1}{1/\lambda_{air} + \frac{\rho\,(1/\lambda_S - 1/\lambda_{air})}{\rho_S}} \quad (18)$$

- Parallel Model:

$$\lambda_B = \lambda_{air} + \frac{\rho}{\rho_S}(\lambda_S - \lambda_{air}) \quad (19)$$

- Krischer Model (Dietrich et al., 2010): (semi empirical model, mixing series and parallel (weighted harmonic average of the Series and Parallel models- $0<f<1$)

$$\lambda_B = \left[f * (1/\lambda_{air} + \frac{\rho\,(1/\lambda_S - 1/\lambda_{air})}{\rho_S}) + (1-f)/\lambda_{air} + \frac{\rho}{\rho_S}(\lambda_S - \lambda_{air})\right]^{-1} \quad (20)$$

- Self Consistent Model (Bruggeman, 1935):

$$(\frac{\rho}{\rho_S})\frac{\lambda_S - \lambda_B}{\lambda_S - 2\lambda_B} + (1 - \frac{\rho}{\rho_S})\frac{\lambda_{air} - \lambda_B}{\lambda_{air} - 2\lambda_B} = 0 \quad (21)$$

Where λ_B , λ_S and λ_{air} are respectively the thermal conductivity of the packing at a given density, that of the cell-wall skeleton and that of air (λ_{air} =26 mW.m^{-1}K^{-1}).

Considering the internal structure of hemp particles, *i.e.,* of almost only longitudinal capillaries, it is theoretically possible to correlate the conductivity along a particle $\lambda_{P//}$and the conductivity of the cell walls λ_S , using a parallel model:

$$\lambda_{P//} = \lambda_{air} + \frac{\rho_P}{\rho_S}(\lambda_S - \lambda_{air}) \quad (22)$$

Pierre and Carin (2019) measured the conductivity of individual hemp shiv particles by infrared thermography. They found $\lambda_{P//}$= 124±23 mW.m^{-1}K^{-1} on particles of density ρ_P =265±15 kg.m^{-3}. Applying Eq. (22) with ρ_S=1454 kg.m^{-3} and λ_{air} =26 mW.m^{-1}K^{-1} gives a value λ_S=564±126 mW.m^{-}

795 $^{1}K^{-1}$ for the conductivity of the cell wall skeleton. The models of Eq. (18) to (21) are applied with this

796 value, and plotted in Fig. 12.

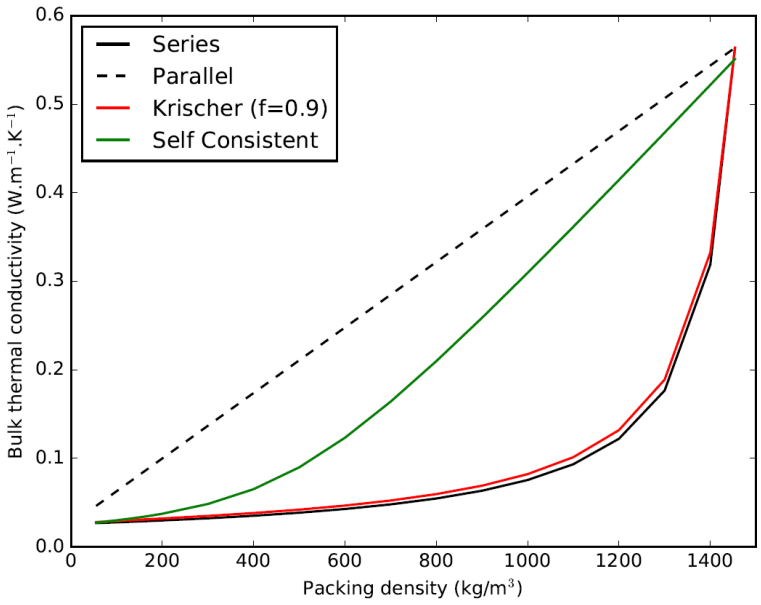

797

798 Figure 12. Evolution of the theoretical conductivity of hemp shiv packing, according to four models

799 of the literature (ρ_S=1454 kg.m^{-3} ; λ_{air} =26 mW.m^{-1}K^{-1} ; λ_S=564 mW.m^{-1}K^{-1})

800

801 It can be observed that, except for the Parallel Model, the bulk conductivity varies very slightly

802 between 60 and 160 kg.m^{-3}, *i.e.,* the maximum packing density that can be reached by hand on dry

803 shiv (see compacted bulk densities, Table 5).

804 Another way to evaluate the thermal conductivity of a hemp shiv packing is to consider the particle

805 conductivity in the models and develop a 2-scale approach. The difficulty is that the hemp particles

806 are orthotropic, or at least transverse isotropic from a thermal point of view. In any case, by

807 applying the Series model to a particle, the transverse conductivity of a particle can be estimated:

808 $$\lambda_{P\perp} = \frac{1}{1/\lambda_{air} + \frac{\rho_P\,(1/\lambda_S - 1/\lambda_{air})}{\rho_S}} = 31 \text{ mW.m}^{-1}\text{K}^{-1} \quad (23)$$

809 This value is certainly a lower boundary of $\lambda_{P\perp}$, as it considers perfectly parallel layers of air and

810 solid, without any thermal bridges. Similar measurements on balsa (Carré and Le Gall, 1990;

811 Pierre and Carin, 2019), in the longitudinal and transverse directions showed a ratio of about ½

812 between longitudinal conductivity and transverse conductivity. Considering that the skeleton's

structures of balsa and hemp shiv are similar, this could lead to $\lambda_{P\perp}$~ 62 mW.m^{-1}K^{-1}. In her PhD thesis, Cerezo (2005) deduced a mean value of 102 mW.m^{-1}K^{-1} for hemp shiv particles using an inverse analysis applied to her experimental values on lime and hemp concrete with a spherical self-consistent model. This value lies between $\lambda_{P\perp}$(Eq. (23)) and $\lambda_{P//}$, which is consistent. In order to take into account the transverse isotropy of particles, the Krischer model can be reformulated (Eq. (24)).

$$\lambda_B = \left[f * (1/\lambda_{air} + \frac{\rho\,(1/\lambda_{P\perp} - 1/\lambda_{air})}{\rho_P}) + (1-f)/\lambda_{air} + \frac{\rho}{\rho_P}(\lambda_{P//} - \lambda_{air}) \right]^{-1} \quad (24)$$

In a loose packing state, the particles are almost randomly oriented (geometric isotropy of the packing of particles). But under compression, the particles are increasingly oriented to lie flat, and tend towards a transverse isotropy, as shown by Williams et al. (2016, 2017) on lime and hemp composites. The weight coefficient f in Eq. (24) can then vary with the overall orientation of the particles, from an isotropic behaviour of the loose packing (f=0.5) towards a packing of almost parallel layers at the very end of the rearrangement phase (see section 3.2.3) for which f is chosen equal to 1. A linear evolution of f as a function of packing density is proposed. The model of Eq. (24) is then plotted in Fig. 13, and compared with the experimental results.

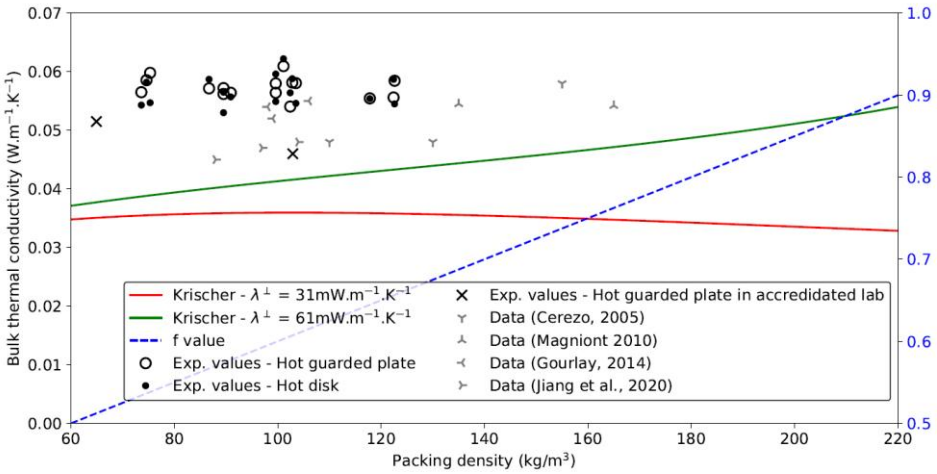

Figure 13. Krischer Model, considering the anisotropy induced by compaction (ρ_P=265kg.m^{-3} ; λ_{air} =26 mW.m^{-1}K^{-1} ;$\lambda_{P//}$=124 mW.m^{-1}K^{-1} ; “Series Model” : $\lambda_{P\perp}$=31 mW.m^{-1}K^{-1} “Balsa ratio” :$\lambda_{P\perp}$=62 mW.m^{-1}K^{-1})

The experimental values of the present study are not close to those of the modelling, probably due to three main reasons:

- at low densities, convection and radiation could affect the thermal properties. This should not be predominant in the range of density and sample thickness considered here, but the proposed model overlooks these phenomena;
- the values taken from (Pierre and Carin, 2019) were not obtained in the same room conditions and on the same shiv than in the present study, and strong assumptions were made on transverse values of the thermal conductivity of particles, and on the weight coefficient f;
- the measurement method and the sample conditioning can affect the experimental results, as shown by Colinart et al. (2019).

The real average thermal conductivity of the skeleton could be estimated by an inverse analysis. However, this approach is risky because the experimental data are highly scattered. A clear conclusion cannot be drawn regarding the best model for the thermal conductivity of hemp shiv, due to the large scatter in the experimental data and the range of uncertainty in the model input data. However, such an approach illustrates how porosity can be used in physical models to understand in more depth the thermal behaviour of hemp shiv packing.

3.2.5. Acoustic properties

The densities resulting from the acoustic characterisation are presented in Table 5. Compared to Geopyc and Hg-intrusion particle density values, it appears that acoustic densities are

852 systematically much higher. However, the acoustic densities show exactly the same tendencies as
853 the other methods concerning particle size and immersion effects, described above in 3.1.1.

854 These observations indicate that the acoustic density does not correspond to the particle density.
855 Practically, this means that acoustic dissipation occurs not only in interparticle porosity, but also in
856 part of the intra-particle porosity. The pore size distribution measured by mercury intrusion and
857 presented in Fig. 5 highlighted the existence of two groups of pores. It is thus likely that at least a
858 part of the bigger pores (measuring about 10 to 50 µm) also contribute to the sound dissipation in
859 hemp shiv.

860 To develop this theory, a comparison was made between acoustic data and modelling approaches
861 based on four hypotheses:

862 - H1: Double porosity without coupling as described in (Glé et al., 2012), 1 scale of porosity -
863 φ_{acou};
864 - H2: Double porosity without coupling: 1 scale of porosity - φ_I: This hypothesis is similar to
865 the first approach but considers that only inter-particle pores participate in acoustic
866 dissipation. $\varphi_I = 1 - \frac{\rho_B}{\rho_P}$ is different than φ_{acou} and is deduced here from the Geopyc
867 envelope density;
868 - H3: Double porosity with coupling: 2 scales - φ_I + φ_P: here, all open pores participate in the
869 dissipation, φ_I (deduced from the Geopyc particle density) as well as φ_P calculated as the
870 difference (in volume) between the open porosity $\varphi_{N_2} = 1 - \frac{\rho_B}{\rho_{N_2}}$ and the interparticle
871 porosity φ_I, so that $\varphi_P = \frac{\varphi_{N_2} - \varphi_I}{1 - \varphi_I}$. The model presented by (Olny and Boutin, 2003) is
872 applied.
873 - H4: Partial double porosity with coupling: 2 scales - φ_I + × φ_P : This case is a derivation of
874 the previous case, where $\eta \times \varphi_P$ corresponds to the portion of φ_P participating in the sound
875 dissipation, a portion fixed at 50%.
876

These four hypotheses are illustrated by the schematic given in Fig. 14.

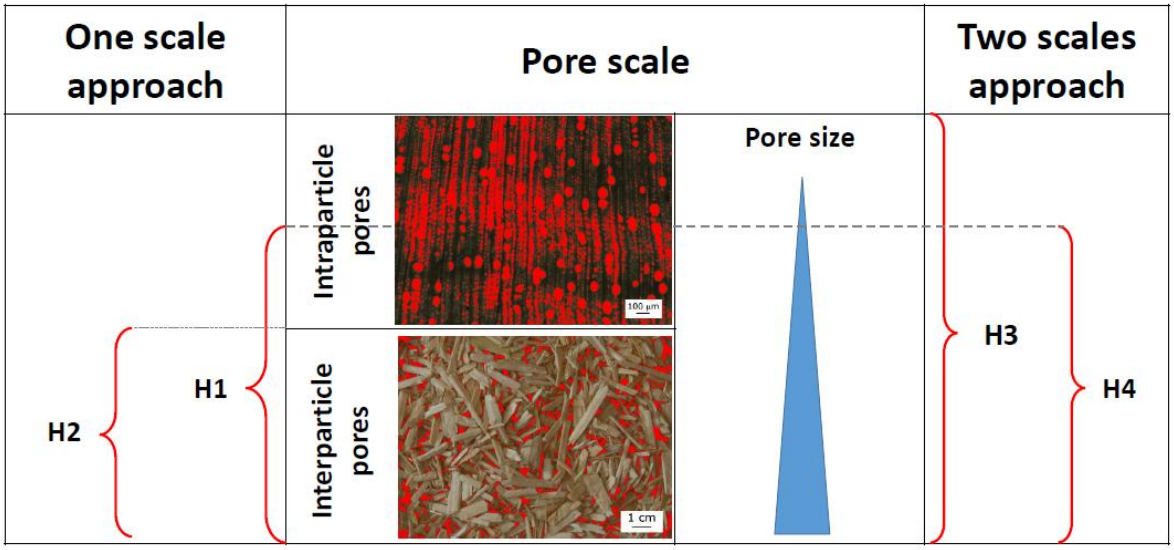

Figure 14. Illustration of the four modelling assumptions

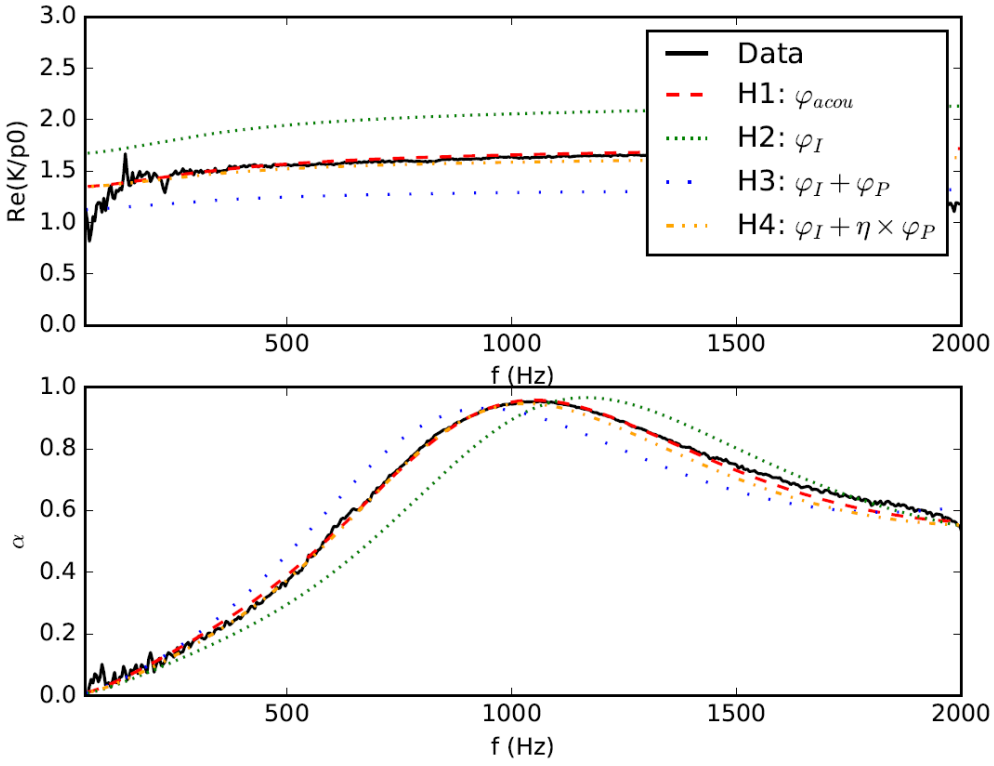

Figure 15. Comparison between acoustic data for hemp shiv L12 (130 kg.m^{-3}) and modelling for the real part of the bulk modulus (top) and for the sound absorption coefficient (bottom)

The real part of the bulk modulus is a property of the material that is related to thermal effects in acoustic dissipation (Allard and Atalla, 2009). This property is mainly related to the porosity of the material, and ranges between two asymptotic values, $K = \frac{p_0}{\varphi}$ (at low frequency) and $K = \gamma \frac{p_0}{\varphi}$ (at high frequency). This acoustic data as well as sound absorption α are plotted versus frequency and compared to experimental data for hemp shiv L12 (130 kg.m^{-3}) in Fig. 15. It can be observed that two of the four hypotheses proposed can be clearly distinguished from the reference data. The approach based on φ_I only gives an overestimate of $Re(K)$. On the contrary, the approach based on φ_I + φ_P underestimates these data. The reason is that the contributing porosity is respectively under- and overestimated with these hypotheses. In this context, the partial double porosity approach (H4) with coupling seems to be satisfactory. The reference approach (H1, described by Glé et al. (2012)) is also close to the data, but relies on an acoustic inversion of the effective porosity.

The results regarding the sound absorption coefficient are in line with the previous remarks. The two best approaches predict α with a deviation lower than 5% compared to the data.

4. Conclusion

This paper aimed to investigate the densities and microstructures of plant particles used for bio-based building applications. It combines experimental determination of the density at three scales, *i.e.* packing, particle and skeleton of hemp shiv. Analyses were carried out regarding the implications of these characteristics on the physical behaviour of the material. The work focused on eight shiv having the same origin but different particle size distribution and aging.

The cross-analysis of different methods proved to be relevant to fully characterise these materials. Powder pycnometry appeared to be one of the most efficient and representative methods to

907 characterise particle density. Mercury intrusion porosimetry enabled the validation of the range of
908 densities but with stronger limitations due to the "ink-bottle" effects expected for plant particles.
909 Finally, X-ray computed tomography enabled the characterisation of the particles individually and
910 the validation the range of data from the two other methods. Because image acquisition and
911 processing are very time-consuming, it was therefore not appropriate for the statistical and
912 systematic assessment of particle density, but more suited for local microstructure
913 characterisation.

914 It has been demonstrated that smaller particles have higher packing and particle densities,
915 probably due to the original position of particles in the stems. In addition to this, particles aged
916 through immersion in water presented a significant evolution of their microstructure, leading to
917 lower packing and particle densities and higher skeletal density. This evolution is related to the
918 combined effects of particles swelling with the opening of intra-particle pores. It would be
919 interesting to complement these results by direct tomographic observations at high resolution to
920 characterise the morphology and the evolution of porosity.

921 The links of these densities with the physical properties were explored. Correlations were found
922 between water absorption and open porosity, compression behaviour and the three scales of
923 densities, and between acoustic dissipation and intra- and inter-particle porosities. Theoretical links
924 also exist with water adsorption and thermal dissipation, but they could not be demonstrated
925 experimentally.

926 These results thus facilitate an interesting advance in the knowledge of the microstructure of plant
927 particles, which could be used to optimise the formulation of materials derived from hemp shiv,
928 identify their extreme limits in terms of density, and propose better modelling of their physical
929 performance in buildings.

5. Acknowledgments

This study is a part of the ECO-TERRA project (Development of light earth construction materials for efficient green buildings), with the support of ADEME.

The authors would like to thank Philippe Gadonneix (Université de Lorraine, IJL) for additional measurements using Autotap, Geopyc, Accupyc and Autopore devices, and Patrick Aimedieu (Laboratoire Navier) for his valuable advice on the acquisition of the X-ray tomographic images.

6. References

NF V 18-122 - Aliments des animaux - Détermination séquentielle des constituants pariétaux - Méthode par traitement aux détergents neutre et acide et à l'acide sulfurique.

Allard, J.F., Atalla, N., 2009. Propagation of sound in porous media: Modelling sound absorbing materials, second edition. Wiley.

Amziane, S, Arnaud, L. (Eds.), 2012. Bio-aggregate-based Building Materials: Applications to Hemp Concretes, Wiley.

Amziane, S., Collet, F. (Eds.), 2017. Bio-aggregates Based Building Materials, Vol. 23 of RILEM State-of-the-Art Reports, Springer Netherlands, Dordrecht.

Amziane, S., Collet, F. (Eds.), 2018. Bio-aggregates Based Building Materials: State-of-the-Art Report of the RILEM Technical Committee 236-BBM.

Beaugrand, J., Nottez, M., Konnerth, J., Bourmaud, A., 2014. Multiscale analysis of the structure and mechanical performance of woody hemp core and the dependence on the sampling location, Ind. Crop. Prod. 60, 193-204.

950 Bennai, F., El Hachem, C., Abahri, K., Belarbi, R., 2018. Microscopic hydric characterization of
951 hemp concrete by X-ray microtomography and digital volume correlation, Constr. Build. Mater. 188,
952 983-999.

953 Van den Berg, C., Bruin, S., 1981. Water activity and its estimation in food systems. Water Activity:
954 Influences on Food Quality, L.B. Rockland & G.F. Stewart, 147–177. Academic Press, New York.

955 Breck, D., 1974. Zeolite Molecular Sieves, 1 ed.; John Wiley & Sons: New York.

956 Brisard, S., Serdar, M., Monteiro, P.J.M., 2020. Multiscale X-ray tomography of cementitious
957 materials: A review. Cem. Concr. Res. 128, 105824.

958 Bruggeman, D., 1935. Berechnung verschiedener Physikalischer Konstanten von heterogenen
959 Substanzen, Annalen Physik 24, 636-679.

960 Cappelletto, P., Brizzi, M., Mongardini, F., Barberi, B., Sannibale, M., Nenci, G., Poli, M., Corsi, G.,
961 Grassi, G., Pasini, P., 2001. Italy grown hemp yield, composition and cannabinoid content. Ind.
962 Crop. Prod. 13 (2), 101-113.

963 Carré, P., Le Gall, R., 1990. Définition et détermination des conductivités thermiques dans les
964 structures C.V.R. – balsa, Rev. Gén. Therm. Fr. 340, 211–215.

965 Castel, Y., Amziane, S., Sonebi, M., 2016. Durabilité du béton de chanvre : résistance aux cycles
966 d'immersion hydrique et séchage. 1ère Conférence EuroMaghrébine des BioComposites,
967 Marrakech, Maroc.

968 Cerezo, V., 2005. Propriétés mécaniques, thermiques et acoustiques d'un matériau à base de
969 particules végétales: approche expérimentale et modélisation théorique, PhD thesis, INSA,
970 ENTPE, Lyon.

971 Ceyte, I., 2008. Béton de chanvre, définition des caractéristiques mécaniques de la chènevotte,
972 Master thesis, ENTPE.

973 Chiasson-Poirier, L., Lecompte, T., Hellouin de Menibus, A., 2020. Static and long term
974 compression behavior of hemp shiv for floating floor application, Constr. Build. Mater. 268, 121220.

975 Collet, F., Prétot, S., 2014. Thermal conductivity of hemp concretes: variation with formulation,
976 density and water content. Constr. Build. Mater. 65, 612-619.

977 Colinart, T., Vinceslas, T., Lenormand, H., Hellouin de Menibus, A., Hamard, E., Lecompte, T.,
978 2019. Hygrothermal properties of light-earth building materials. J. Build. Eng. 29, 101134.

979 Cooper, A.R., Eaton, L.E., 1962. Compaction behavior of several ceramic powders. J. Am. Ceram.
980 Soc. 45 (3), 97-101.

981 Delannoy, G., Marceau, S., Glé, P., Gourlay, E., Gueguen-Minerbe, M., Diafi, D., Nour, I.,
982 Amziane, S., Farcas, F., 2018. Aging of hemp shiv used for concrete. Mater. Des. 160, 752–762.

983 Delannoy, G., Marceau, S., Glé, P., Gourlay, E., Gueguen-Minerbe, M., Diafi, D., Amziane, S.,
984 Farcas, F., 2020. Impact of hemp shiv extractives on hydration of Portland cement. Constr. Build.
985 Mater. 244, 118300.

986 Dietrich, B., Schell, G., Bacharsky, E.C., Oberacker, R., 2010. Determination of the thermal
987 properties of Ceramic sponges, Int. J. Heat Mass Transf. 53, 198-205.

988 Ehrnrooth, E.M.L., 1984. Change in Pulp Fibre Density With Acid-Chlorite Delignification, J. Wood
989 Chem. Technol. 4 (1), 91-109.

990 Evrard, A., 2008. Transient hygrothermal behavior of Lime-Hemp Materials, Ph.D. thesis,
991 Université Catholique de Louvain.

992 Fares, H., 2014. Paramètres de composition des mélanges de particules de chènevotte pour
993 l'élaboration de béton de chanvre, Montpellier, France

994 Fotsing, E.R., Lecompte, T., Ross, A., 2017. Acoustic properties of lime/hemp concrete produced
995 by compression molding, Second ICBBM, Clermont-Ferrand.

996 Glé, P., Gourdon, E., Arnaud, L., 2012. Modelling of the acoustical properties of hemp particles.
997 Constr. Build. Mater. 37, 801-811.

998 Glé, P., 2013. Acoustique des matériaux du bâtiment à base de fibres et particules végétales –
999 Outils de caractérisation, modélisation et optimisation. PhD Thesis, MEGA ENTPE, Vaulx-en-Velin.

1000 Glé, P., Gourlay, E., 2015. Rapport de recherche MABIONAT, Étude de l'influence de la teneur en
1001 eau et du vieillissement sur les performances acoustiques et thermiques des matériaux
1002 biosourcés.

1003 Gourlay, E., 2014. Caractérisation expérimentale des propriétés mécaniques et hygrothermiques
1004 du béton de chanvre : détermination de l'impact des matières premières et de la méthode de mise
1005 en œuvre, PhD thesis, ENTPE, Lyon.

1006 Gouillart, E., Nunez-Iglesias, J., Van der Walt, S., 2016. Analyzing microtomography data with
1007 Python and the scikit-image library. Adv. Struct. Chem. Imaging 2 (1), p. 18.

1008 Ingrao, C., Lo Giudice, A., Bacenetti, J., Tricase, C., Dotelli, G., Fiala, M., Siracusa, V., Mbohwa,
1009 C., 2015. Energy and environmental assessment of industrial hemp for building applications: A
1010 review, Renew. Sust. Energ. Rev. 51, 29-42.

1011 Iwase, T., Izumi Y., Kawabata, R. A., 1998 new measuring method for sound propagation constant
1012 by using sound tube without any air spaces back of a test material. Internoise 98, Christchurch,
1013 New Zealand.

1014 Jiang, Y., Lawrence, M., Ansell, M.P., Hussain, A., 2018. Cell wall microstructure, pore size
1015 distribution and absolute density of hemp shiv, R. Soc. open sci. 5, 171945.

1016 Jiang, Y., Lawrence, M., Zhang, M., Cui, J., 2020. Industrial bio-based plant aggregates as hygric
1017 and insulating construction materials for energy efficient building, Front. Chem. Sci. Eng.

1018 Jones, W.D., 1960. Fundamental Principle of Powder Metallurgy, Edward Arnold Publisher Ltd,
1019 London, UK.

1020 Kinnane, O., Reilly, A., Grimes, J., Pavia, S., Walker, R., 2016. Acoustic absorption of hemp-lime
1021 construction, Constr. Build. Mater. 122, 674-682.

1022 Laborel-Préneron, A., Magniont, C, Aubert, J.E., 2018. Characterization of Barley Straw, Hemp
1023 Shiv and Corn Cob as Resources for Bioaggregate Based Building Materials, Waste and Biomass
1024 Valorization, 9, 1095-1112.

1025 Lam, P., Sokhansanj, S., Bi, X., Lim, C., Naimi, L., Hoque, M., Mani, S., Womac, A., Ye, X.,
1026 Narayan, S., 2007. Bulk density of wet and dry wheat straw and switchgrass particles, Appl. Eng.
1027 Agric. 24 (3), 351–358.

1028 Lecompte T., 2019. Matériaux biosourcés pour le bâtiment et stockage temporaire de carbone,
1029 Techniques de l'Ingénieur, C8124 v1.

1030 Lenormand, H., Hellouin de Menibus, A., Besnier, J.B., Leblanc, N., 2017. Variability of hemp
1031 shives : study through ibis and chanvrisol projects, ICCBM 2017, Clermont-Ferrand, France.

1032 Lenormand, H., Zmamou, H., Leblanc, N., 2018. Agricultural by-products : variability impact of
1033 characterization protocols on biosourced materials performances, Euromagh 2018, Hammamet,
1034 Tunisie.

1035 Magniont, C., 2010. Contribution à la formulation et à la caractérisation d'un écomatériau de
1036 construction à base d'agroressources, PhD Thesis, Toulouse III.

1037 Maire, E., Withers, P.J., 2014. Quantitative X-ray tomography, International Materials Reviews 59,
1038 1–43.

1039 Mani, S., Tabil, L.G., Sokhansanj, S., 2004. Evaluation of compaction equations applied to four
1040 biomass species, Can. Biosyst. Eng. 46 (3), 55–61.

1041 Meyer, K., Klobes, K.P., 1999. Comparison between different presentations of pore size
1042 distribution in porous materials, Fresenius J. Anal. Chem. 363, 174–178.

1043 Nguyen, T.T, Picandet, V., Carré, P., Lecompte, T., Amziane, S., Baley, C., 2010. Effect of
1044 compaction on mechanical and thermal properties of hemp concrete, Eur. J. Environ. Civ. Eng. 14
1045 (5), 545-560.

1046 Nguyen, T.T., 2010. Contribution à l'étude de la formulation et du procédé de fabrication
1047 d'éléments de construction en béton de chanvre. PhD thesis, Université Bretagne Sud, Lorient.

1048 Nguyen, S.T., Tran-Le, A.D., Vu, M.N., To, Q.D., Douzane, O., Langlet, T., 2016. Modeling thermal
1049 conductivity of hemp insulation material: A multi-scale homogenization approach, Build. Environ.
1050 107, 127-134.

1051 Nozahic, V., 2012. New eco-conception approach for biobased concrete based on the
1052 understanding of the binder/granulate interface : application to hemp and sunflower with a lime-
1053 pumice binder, Ph.d. thesis, Blaise Pascal University, Clermont Ferrand.

1054 Olny, X., Boutin, C., 2003. Acoustic wave propagation in double porosity media. J. Acoust. Soc.
1055 Am. 114 (1), 73–89.

1056 Onoda, G.Y., Liniger, E.G., 1990. Random loose packings of uniform spheres and the dilatancy
1057 onset, Phys. Rev. Lett. 64, 2727.

1058 Pierre, T., Carin, M., 2019. Characterization of the thermal properties of millimeter-sized insulating
1059 materials, Int. J. of Therm. Sci. 135, 247-255.

1060 Pittau, F., Krause, F., Lumia, G., Habert, G., 2018. Fast-growing bio-based materials as an
1061 opportunity for storing carbon in exterior walls, Build. Environ. 129, 117-129.

1062 Ribeiro, A., Pochart, P., Day, A., Mennuni, S., Bono, P. Baret, J.L., Spadoni, J.L., Mangin, I., 2015.
1063 Microbial diversity observed during hemp retting. Appl. Microbiol. Biotechnol. 99, 4471–4484.

1064 Schindelin, J., Arganda-Carreras, I., Frise, E., Kaynig, V., Longair, M., Pietzsch, T., Preibisch, S.,
1065 Rueden, C., Saalfeld, S., Schmid, B., Tinevez, J.Y., White, D.J., Hartenstein, V., Eliceiri, K.,
1066 Tomancak, P., Cardona, A., 2012. Fiji: an open-source platform for biological-image analysis. Nat.
1067 Methods 9, 676–682.

1068 Seeling, P., Wulff, J., 1946. Pressing operation in fabrication of articles by powder metallurgy,
1069 Trans. Am. Inst. Min. Metall. Eng. 166, 492–505.

1070 Sun, C., 2005. True density of microcrystalline Cellulose, J. Pharm. Sci. 94 (10), 2132-2134.

1071 Thygens, A., Liu, M., Meyer, A., Daniel, G., 2013. Hemp fibres: enzymatic effect of microbiol
1072 processing on fibre bundle structure. Proceeding of the 34th Riso International symposium of
1073 materials science, 373-380.

1074 Tran-Le, A.D., Nguyen, S.T., Langlet, T., 2019. A novel anisotropic analytical model for effective
1075 thermal conductivity tensor of dry lime-hemp concrete with preferred spatial distributions, Energy
1076 Build. 182, 75-87.

1077 Tronet, P., Lecompte, T., Picandet, V., Baley, C., 2014. Study of lime and Hemp composite
1078 precasting by compaction of fresh mix- A Fitted die to measure friction and stress state, Powder
1079 Technol. 258, 285-296.

1080 Tronet, P., Lecompte, T., Picandet, V., Baley, C., 2016. Study of lime hemp concrete (LHC)-Mix
1081 design, casting process and mechanical behavior, Cem. Concr. Compos. 67, 60-72.

1082 Viel, M., Collet, F., Lanos, C., 2018. Chemical and multi-physical characterization of agro-
1083 resources' by-product as a possible raw building material, Ind. Crops Prod. 120, 214-237.

1084 Walker, E.E., 1923. The properties of powders — part VI: the compressibility of powders, Trans.
1085 Faraday Soc. 19 (1), 73-82.

1086 Williams, J., Lawrence, M., Walker, P., 2016. A method for the assessment of the internal structure
1087 of bio-aggregate concretes. Constr. Build. Mater. 116, 45-51.

1088 Williams, J., Lawrence, M., Walker, P., 2017. The influence of the casting process on the internal
1089 structure and physical properties of hemp-lime. Mater. Struct. 50(2), 108.

1090 Zieger, V., Lecompte, T., Hellouin de Menibus, A., 2020. Impact of GHGs temporal dynamics on
1091 the GWP assessment of building materials: A case study on bio-based and non-bio-based walls,
1092 Build. Environ. 185, 107210.

7. Appendix: Acquisition and processing of XRCT images

Image acquisition was performed at Navier laboratory using a XRCT laboratory scanner (Ultratom from RX-Solutions), with a 230 kV micro-focus source Hamamatsu L10801 and a flat-panel detector Varex 4343 DX-I. The tube voltage and the tube current of the source were set to 70 kV and 170 µA, respectively. The frame rate of the detector was set to 1 projection/s and 16 radiographs were averaged at the same angular position to improve the signal-to-noise ratio of the projections. Under these imaging conditions, one scan lasted about 12 hours to acquire 2336 projections over 360°. After reconstruction, it results in a 3D image of about 2000x2000x2500 voxels with a voxel size of 12 µm.

Sub-volumes containing only one particle were manually defined. After conversion in 8-bit integer format, they were processed as follows:

- denoising: a total variation minimisation filter is applied to reduce noise and artefacts while preserving the particle edges;
- segmentation: the grey levels are thresholded above a value determined using the Triangle method. For most particles, the threshold is calculated for the whole 3D image. For a few images presenting artefacts, the thresholding is computed locally on transverse slices. Morphological operations (binary closing, opening and filling holes) are then applied to obtain the final binary image, which isolates the particle, and possible residual parts of EPS beads or adhesive tape, from the rest of the image;
- volume measurement: the connected regions are labelled and their volumes are defined as the number of voxels N associated with their respective labels. The hemp shiv's apparent volume corresponds to the largest region. The volume V in metric units is given by $= Nl^3$, where l is the side length of a voxel.

This procedure has been automatically performed on all particles using Python, relying on NumPy, SciPy, and scikit-image packages (Gouillart et al., 2016). The error in volume measurement has been estimated by analysing the effect of the denoising weight, the grey level threshold and the size of the structuring element used in morphological operations.

The resulting envelopes have been checked visually for all particles. Furthermore, Fig. A.1 shows that the measured apparent densities are consistent with grey levels in particles. In fact, in perfect absorption contrast XRCT images, grey level is usually assumed to vary linearly with the X-ray attenuation coefficient, which increases with material density. Under certain experimental conditions, including equipment and calibration, grey levels can be used directly to estimate the material densities (Maire and Withers, 2014). In this study, the purpose of Fig. A.1 is only to validate the particle density assessment, in particular with regard to extreme values.

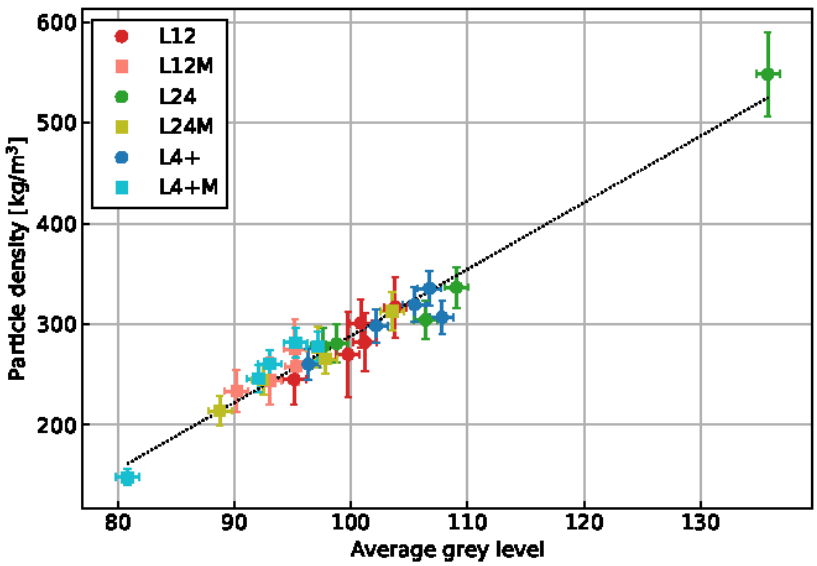

Figure A.1. Particle densities calculated from volume and mass measurements as a function of the average grey level within the particles. The uncertainty in the average grey level has been estimated by analysing the effect of thresholding only.